COMMUN. MATH. SCI.
Vol. 11, No. 3, pp. 651–678

A RELAXATION METHOD FOR THE PULSATING TRAVELING FRONT SIMULATIONS OF THE PERIODIC ADVECTION DIFFUSION REACTION EQUATIONS*

MIN TANG†

Abstract. In this paper, we propose a new relaxation method to study the pulsating traveling front for the one dimensional space and time periodic advection diffusion reaction equations. By introducing an additional parameter depending on time, the front position is confined around a fixed point, so that this method requires small computational domain. Moreover, the time evolution of this additional parameter gives the traveling velocity automatically, and the results of the original advection diffusion reaction equation can be recovered.

Key words. Space periodic advection diffusion reaction equation, time periodic advection diffusion reaction equation, traveling wave solution, pulsating traveling front, relaxation method.

AMS subject classifications. 65M06, 35C07, 35K57.

1. Introduction

In this paper, we propose a new relaxation method to study the pulsating traveling front for the one dimensional space and time periodic advection diffusion reaction equations. These equations have wide applications in various physical and biological models. For example, the premixed flame propagation in turbulent flows [32], signal propagation along bistable transmission lines, biological invasion [25, 26], and so on.

The space periodic advection diffusion reaction equation is

$$\partial_t u - \partial_x(A(x)\partial_x u) + q(x)\partial_x u = f(x,u), \tag{1.1}$$

with

$$A(x+L) = A(x), \qquad q(x+L) = q(x), \qquad f(x+L,u) = f(x,u). \tag{1.2}$$

Here the coefficients $A(x), q(x) \in C^{1+\alpha}(\mathbb{R})$ for a given $\alpha \in (0,1)$ are independent of time and periodically depend on space. Moreover, there exist some positive constants γ and Γ such that $\gamma < A(x) < \Gamma$. The reaction term $f(x,u): \mathbb{R}\times\mathbb{R} \to \mathbb{R}$ is of class C^α in x and locally in u [19]. When $q(x) \equiv 0$, $f(x,u) = u(\mu(x) - u)$ and $A(x)$, $\mu(x)$ are piecewise constants, this is called a patch model, which models the biological invasion when the environment is composed by alternating favorable and less favorable patches [25].

When the coefficients depend periodically on time instead of space, the general form of time periodic advection diffusion reaction equation is

$$\partial_t u - \partial_x(A(t)\partial_x u) + q(t)\partial_x u = f(t,u) \tag{1.3}$$

with

$$A(t+T) = A(t), \qquad q(t+T) = q(t), \qquad f(t+T,u) = f(t,u). \tag{1.4}$$

$A(t)$, $q(t)$, and $f(t,u)$ have similar regularity as in the space periodic equation, but with respect to time. The time periodic dependence reflects the effects of certain

*Received: April 4, 2012; accepted (in revised form): July 23, 2012. Communicated by Jack Xin.
†Institute of Natural Sciences, Department of Mathematics and MOE-LSC, Shanghai, Jiao Tong University, Shanghai, 200240, P.R. China (tangmin@sjtu.edu.cn).

"seasonal" variations. When $A(t)$ is a constant and $f(t,u)$ is independent of time, the existence of pulsating front solutions has already been studied analytically in [17, 18].

The equations (1.1), (1.3) are, on the one hand, an extension of the homogeneous reaction diffusion equation

$$\partial_t u = \partial_{xx} u + f(u), \qquad u:(x,t)\to\mathbb{R} \text{ for } x,t\in\mathbb{R}, \tag{1.5}$$

and, on the other hand, the simplest form of the scalar advection diffusion reaction equation with nonconstant coefficients. Equation (1.5) is used to describe the wave propagation for genetics, the invasion of species and many other phenomena in physics and biology. A lot of work in the literature investigate the behavior of (1.5), which exhibits traveling wave solutions [6, 7]. Recently the more general forms (1.1) and (1.3), which take into account heterogeneous environments, attract more and more effort. The tendency to diffuse, transport or birth and die may be different from place to place, or from time to time. Therefore the diffusion, advection, and reaction coefficients depend on space or time. Such models were first studied rigorously by probabilistic methods in [10, 11]. Later on, a generalized definition of traveling waves called pulsating traveling front was proposed for these periodic environment models [25, 26, 31, 32], for which both the front shape and the traveling velocity change periodically in time. The first proof of pulsating traveling front is given by J. Xin in [31, 32], and afterwards H. Berestycki, F. Hamel, J. Nolen, and J. Xin etc. have done a lot of work about the existence and stability of the pulsating traveling front [5, 18].

Previous numerical methods solve equation (1.1) or (1.3) directly, and let the fronts propagate. There are two difficulties about this approach: firstly, it may take a long time for u to converge to a pulsating traveling front, which requires a large computational domain for propagation; secondly, even after u has converged to a pulsating traveling front, the front velocity is not easy to find numerically. Either we let the front propagate for a long time and calculate the average velocity, or we find two successive time points that possess the same front shape, which is not a easy task when the front profiles change periodically but the profile differences are quite small or the period is small. In this paper, we propose a new relaxation method that can get rid of both difficulties: the front position is confined around a fixed point in the computational domain after some time, so that a much smaller computational domain is required; the front velocity can be found automatically during the calculation. Moreover, we can recover the solution of the original time evolution equation.

The traveling wave solution can be viewed as a pulsating traveling front with period being any positive constant. In [27], a relaxation method for the traveling wave simulations is proposed. Take $f[u]=u(1-u)$ in (1.5) as an example; the key idea is to introduce an additional interior fixed point to get rid of the transit invariance. More precisely, we construct the traveling wave solution by first finding a specific σ^{B*} and the corresponding v^{B*} that satisfy

$$\begin{cases} -\sigma^{B*}\partial_x v^{B*} = \partial_{xx} v^{B*} + f(v^{B*}), \\ v^{B*}(x_l)=1, \quad v^{B*}(x_r)=0, \quad v^{B*}(0)=\epsilon, \\ \epsilon\in(0,1), \qquad x_l<0, \quad x_r>0, \end{cases} \tag{1.6}$$

and then passing to the limit $x_l\to-\infty$, $x_r\to+\infty$ [7]. Here the super script "B" indicates that we are considering the solution in a bounded domain. The introduction of ϵ not only provides us an additional parameter to adjust σ^{B*}, but also avoids the translation invariance when $x_{l,r}\to\pm\infty$. In [27], this additional condition $v^{B*}(0)=\epsilon$ is

imposed through an operator $\mathfrak{P}: v^{B*} \to \sigma^{B*}$, which is not unique. Then, the solution of (1.6) is the steady state of

$$\begin{cases} \partial_t v^B - \sigma^B \partial_x v^B = \partial_{xx} v^B + f(v^B), \\ \sigma^B = \mathfrak{P}(v^B), \\ v^B(x_l,t) = 1, \qquad v^B(x_r,t) = 0, \end{cases} \tag{1.7}$$

with

$$\mathfrak{P}(v^B) = \begin{cases} \frac{1}{\epsilon}\Big(\partial_x v^B|_0^{x_r} + \int_0^{x_r} f(v^B)\Big), & \text{when } \sigma^{B*} > 0, \\ \frac{1}{1-\epsilon}\Big(\partial_x v^B|_{x_l}^0 + \int_{x_l}^0 f(v^B)\Big), & \text{when } \sigma^{B*} < 0. \end{cases} \tag{1.8}$$

Starting from an initial v^B, we can decide σ^B through $\mathfrak{P}(v^B)$, and then by the time evolutionary equation we can calculate v^B at the next time step, and also σ^B at the next time step. If σ^B converges to a constant and v^B to a steady state when $t \to +\infty$, σ^{B*}, v^{B*} in (1.6) are found, so is the traveling wave solution by letting $x_{l,r} \to \pm\infty$. This provides us a relaxation method for the traveling wave simulations. To achieve the convergence, different operators $\mathfrak{P}$ are used for different signs of σ^{B*}. The necessity of these different choices has been justified both analytically and numerically for the traveling wave simulations.

In this present paper, we are going to extend this relaxation method to the simulations of one dimensional pulsating traveling fronts. Formally, we construct a new parabolic system similar to (1.7), whereas the coefficients are no longer constant but periodic in space or time. If the solution of (1.1) or (1.3) converges to a pulsating traveling front as time goes on, we show that after some time, the solution (σ^B, v^B) of the new system changes periodically in time. The introduction of σ^B can, on the one hand, confine the front position around a fixed point, so that it reduces the computational cost, and, on the other hand, give the periods of time and space, and the traveling velocity.

It is natural to assume that the coefficients A, q, and the reaction term f simultaneously depend on time and space. However, due to the degeneracy of the parabolic equation, the spatial-temporal periodic case introduces more difficulties about the definition of the pulsating fronts, the form of the limiting states, etc. Some recent efforts have attempted to understand this more general case [20, 21], yet in this paper we focus ourselves on the space periodic equation (1.1) and time periodic equation (1.3).

This paper is organized as follows. Section 2 gives the definition of pulsating traveling front, explains the basic idea of the relaxation method and shows why this relaxation approach can capture and verify the pulsating traveling front. The details of the operator's choice, the boundary conditions, and discretizations are discussed in Sections 3 and 4, respectively for the space periodic equation (1.1) and time periodic equation (1.3). In Section 5, we demonstrate the efficiency of our scheme by three numerical examples, two for the space periodic case and one for time periodic case. Finally, we conclude in Section 6.

2. Pulsating traveling front

In this paper, we are interested in a specific kind of solutions of (1.1) and (1.3) called pulsating traveling fronts. There are two equivalent definitions.

DEFINITION 2.1. *A pulsating traveling front of speed c in one space dimension that connects $p(x)$ $(p(t))$ to 0 is a solution $u(x,t)$ that satisfies the following: $u(x,t) \to 0$*

as $x\to+\infty$, $u(x,t)\to p(x)$ *(space periodic case) or* $u(x,t)\to p(t)$ *(time periodic case) as* $x\to-\infty$ *and* $\forall x,t\in\mathbb{R}$, $u(x,t+\frac{L}{c})=u(x-L,t)$ *(space periodic case) or* $u(x,t+T)=u(x-cT,t)$ *(time periodic case).*

DEFINITION 2.2. *[21] A function* $u(x,t)$ *is a pulsating traveling front of speed* c *that connects* $p(x)$ $(p(t))$ *to* 0 *if it can be written as* $u(x,t)=\phi(x-ct,x)$ $(u(x,t)=\phi(x-ct,t))$, *where* $\phi(x-ct,x)$ $(\phi(x-ct,t))$ *is periodic of period* L *in its second variable. We ask the boundary conditions of* ϕ *to satisfy*

$$\textit{Space periodic case}\begin{cases}\phi(y,x)\to p(x), & \textit{when } y\to-\infty,\\ \phi(y,x)\to 0, & \textit{when } y\to+\infty,\end{cases}$$

or

$$\textit{Time periodic case}\begin{cases}\phi(y,t)\to p(t), & \textit{when } y\to-\infty,\\ \phi(y,t)\to 0, & \textit{when } y\to+\infty.\end{cases}$$

The equivalence of the above two definitions can be easily seen from

$$u\Big(x,t+\frac{L}{c}\Big)=\phi(x-L-ct,x),\qquad u(x-L,t)=\phi(x-L-ct,x-L),$$

or

$$u(x,t+T)=\phi(x-ct-cT,t+T),\qquad u(x-cT,t)=\phi(x-cT-ct,t).$$

Though the pulsating traveling front that connects $p(x)$ $(p(t))$ to 0 does not exist for general choices of A, q, and f in (1.1) ((1.3)), it is found analytically for various cases [4, 28, 29, 30]. For the combustion reaction such that $f(x,u)$ is Lipschitz continuous with respect to u and there exists $\theta\in(0,1)$ such that

$$f(x,u)=0\quad\text{for } u\in(0,\theta);\qquad f(x,u)>0\quad\text{for } u\in(\theta,1);\qquad f(x,1)=0;\quad f'(x,1)<0,\tag{2.1}$$

and the positive nonlinear-reaction case such that

$$f\ge 0,\qquad f(x,0)=f(x,1)=0,\qquad f(x,s)>0,\quad\text{for } s\in(0,1),\tag{2.2}$$

the existence of pulsating traveling front that connects $u\equiv 1$ to $u\equiv 0$ has already been shown for space periodic equation (1.1) in [2, 32]. The extension to the time periodic equation is proved in [9]. For both combustion and positive reaction, f does not change its sign, while when f changes its sign, the model can be used in population dynamics, in which the sign of f indicates that the environment can change from favorable to unfavorable. The bistable reaction is the most studied sign changing case, where the pulsating traveling fronts do not always exist [1, 33].

In order to simulate these generalized traveling fronts, similar to [27], we introduce an additional function $\sigma(t)$, whose effect is to capture the front velocity. We consider the system

$$\begin{cases}\partial_t v-\sigma(t)\partial_s v-\partial_s(A(x)\partial_s v)+q(x)\partial_s v=f(x,v),\\ \sigma(t)=\mathfrak{P}(v),\\ x=s+\int_0^t\sigma(\tau)\,d\tau\end{cases}\tag{2.3}$$

for the space periodic case and

$$\begin{cases}\partial_t v-\sigma(t)\partial_s v-\partial_s(A(t)\partial_s v)+q(t)\partial_s v=f(t,v),\\ \sigma(t)=\mathfrak{P}(v)\end{cases}\tag{2.4}$$

for the time periodic case. Here $\mathfrak{P}$ is an operator on v that will be specified later. Comparing (1.1) and (2.3) ((1.3) and (2.4)), if $u(x,t)$ is the solution of (1.1) ((1.3)), then

$$v(s,t)=v(x-\int_0^t \sigma(\tau)\,d\tau,t)=u(x,t) \tag{2.5}$$

satisfies (2.3) ((2.4)).

The crucial idea of our numerical scheme is based on the observation that, if $(v(s,t),\sigma(t))$ becomes periodic in time as time goes on, then $u(x,t)$ converges to a pulsating traveling front. More precisely, we have

THEOREM 2.3. *Let $u(x,t)$ be the solution to (1.1) ((1.3)) and let $v(s,t)$ satisfy (2.3) ((2.4)). Assume that $v(s,t)$, $\sigma(t)$ are periodic in t, i.e.*

$$v(s,t)=v(s,t+T),\qquad \sigma(t)=\sigma(t+T),\qquad \text{for } t\geq T_0.$$

Due to (2.5)*, we have $u(x,t+T)=u(x-\int_0^T\sigma(\tau)\,d\tau,t)$ for $t>T_0$ and $u(t)$ is a pulsating traveling front with*

$$L=\int_{T_0}^{T_0+T}\sigma(\tau)\,d\tau,\qquad c=\frac{\int_{T_0}^{T_0+T}\sigma(\tau)\,d\tau}{T}. \tag{2.6}$$

Proof. From (2.5) and the periodicity of $v(s,t)$ in t, when $t>T_0$,

$$\begin{aligned}u(x,t+T)&=v(s,t+T)=v(x-\textstyle\int_0^{t+T}\sigma(\tau)\,d\tau,t+T)=v(x-\int_0^{t+T}\sigma(\tau)\,d\tau,t)\\&=v(x-\textstyle\int_t^{t+T}\sigma(\tau)\,d\tau-\int_0^t\sigma(\tau)\,d\tau,t)=u(x-\int_t^{t+T}\sigma(\tau)\,d\tau,t).\end{aligned}$$

The periodicity of $\sigma(t)$ gives that $\int_t^{t+T}\sigma(\tau)\,d\tau$ is independent of t, thus $u(x,t+T)=u(x-\int_{T_0}^{T_0+T}\sigma(\tau)\,d\tau,t)$.

From Definition 2.1, $u(x,t+T)=u(x-\int_{T_0}^{T_0+T}\sigma(\tau)\,d\tau,t)$ indicates that $u(x,t)$ converges to a pulsating traveling front with the space period and traveling velocity in (2.6). ∎

Therefore, in the subsequent part of this paper, we are going to specify $\mathfrak{P}$ to make $(v(s,t),\sigma(t))$ converge to a solution periodic in time.

REMARK 2.4. According to [28, 29], another definition for pulsating traveling fronts is that $u(x,t)=U(x-\bar{c}(t),t)$, where both the wave profile $U(x,t)$ and wave speed $\bar{c}'(t)$ are almost periodic in t. $\int_0^t\sigma(\tau)\,d\tau$ plays the role of $\bar{c}(t)$, so that if $\bar{c}(t)$ is as in [28], $\sigma(t)$ is not necessarily unique for a pulsating traveling front, but the periods T, L, and velocity c are unique.

REMARK 2.5. For the spatial-temporal periodic case such that

$$\partial_t u-\partial_x(A(x,t)\partial_x u)+\partial_x(q(x,t)u)=f(x,t,u),$$

with

$$\begin{aligned}&A(x,t+T)=A(x,t)=A(x+L,t),\\&q(x,t+T)=q(x,t)=q(x+L,t),\\&f(x,t+T,u)=f(x,t,u)=f(x+L,t,u),\end{aligned}$$

there are some difficulties about the definition of the pulsating traveling fronts. As pointed out in [18], Definition 2.1 implies the existence of some $p,q\in\mathbb{Z}$ such that $c=\frac{pL}{qT}$, which is not satisfactory. If we try to extend Definition 2.2, due to the degeneracy, we get only a weak form as in [21]. Therefore, it is not clear whether we obtain a pulsating traveling front or not, even if $(v(s,t),\sigma(t))$ becomes periodic in t as in Theorem 2.3.

3. Space periodic case

In this section, for the new system (2.3) of the space periodic equation, we explain the proper choices of $\mathfrak{P}$, the general boundary conditions, and discuss the detailed discretizations.

3.1. The new parabolic system. To illustrate the basic idea, we firstly focus ourselves on the combustion reaction (2.1) where the two steady states are known and the front velocity is positive. The numerical method itself can be extended to the cases with unknown steady state and negative front velocity.

On the whole real line, the boundary conditions of the original equation (1.1) with combustion reaction are

$$u(-\infty,t)=1,\qquad u(+\infty,t)=0. \tag{3.1}$$

Therefore, due to (2.5), the boundary conditions for v are also $v(-\infty,t)=1$, $v(+\infty,t)=0$. When $\int_0^L q(x)\,dx=0$, the algorithm on the whole real line for the combustion case is to solve

$$\begin{cases} \partial_t v-\sigma(t)\partial_s v-\partial_s(A(x)\partial_s v)+q(x)\partial_s v=f(x,v), \quad s\in(-\infty,+\infty),\\ \sigma(t)=\frac{1}{\epsilon}\Big(A(x)\partial_s v|_0^{+\infty}-\int_0^{+\infty}q(x)\partial_s v\,ds+\int_0^{+\infty}f(x,v(s,t))\,ds\Big),\\ x=s+\int_0^t\sigma(\tau)\,d\tau,\\ v(-\infty,t)=1,\qquad v(+\infty,t)=0. \end{cases} \tag{3.2}$$

Here we have specified $\mathfrak{P}$ and introduced a parameter $\epsilon\in(0,1)$, whose effect is to fix the front position. We emphasize that it is important to have A, q, and f in (3.2) depend on x instead of s, which allows one to recover $u(x,t)$ from $v(s,t)$ by (2.5).

Since only bounded domains can be used in numerical simulations, we truncate the computational domain by $[s_l,s_r]$ with $s_l<0$, $s_r>0$. Then the problem becomes

$$\begin{cases} \partial_t v^B-\sigma^B(t)\partial_s v^B-\partial_s(A(x)\partial_s v^B)+q(x)\partial_s v^B=f(x,v^B), \quad s\in[s_l,s_r],\\ \sigma^B(t)=\frac{1}{\epsilon}\Big(A(x)\partial_s v^B|_0^{s_r}-\int_0^{s_r}q(x)\partial_s v^B\,ds+\int_0^{s_r}f(x,v^B(s,t))\,ds\Big),\\ x=s+\int_0^t\sigma(\tau)\,d\tau,\\ v^B(s_l,t)=1,\qquad v^B(s_r,t)=0. \end{cases} \tag{3.3}$$

Although $s\in[s_l,s_r]$ is bounded in (3.3), x can be any value on the whole real line. From (1.2), we only need to define $A(x)$, $q(x)$, and $f(x,v)$ for $x\in[0,L]$ and then extend the values to $\mathbb{R}$. Comparing (3.3) with (1.7), (1.8), the relaxation system for traveling wave solutions (1.7), (1.8) with combustion reaction is a special case of (3.3) when A, q, and f are uniform in x.

The combustion case is the simplest one for two reasons. One reason is that the two steady states are known explicitly, and the other is that the traveling velocity is

always positive when $\int_0^L q(x)\,dx=0$ [1]. The two boundary conditions in (3.1) come from the steady state of (1.1) with combustion reaction whereas the specific choice of $\mathfrak{P}(v^B)$ is due to the positivity of c. We will now explain the effect of ϵ and discuss the boundary conditions and operator $\mathfrak{P}$ for more general reaction terms and traveling velocities.

The effect of ϵ

In order to understand the effect of ϵ, here we give some formal explanations when $f(x,u)=g(u)$ is of the combustion type and independent of x. We start from a pulsating traveling front and let it propagate. If $u(x,t)$ is positive, monotonically decreasing in x and increasing in t, the front position at time t can be measured by the value of $\int_0^{+\infty} u(x,t)\,dx$. From (2.5), $v(s,t)$ has a similar front profile as $u(x,t)$. Therefore, if we want to show that the front position of v is confined in a certain interval, we can check whether the value of $\int_0^{+\infty} v(s,t)\,ds$ has uniform upper and lower bounds for all $t>0$.

By substituting the pulsating traveling front (Definition 2.2)

$$u(x,t)=\phi(x-ct,x)\equiv\phi(y,x),\quad y=x-ct\in\mathbb{R},\quad \phi(y,x+L)=\phi(y,x)$$

into the space periodic equation (1.1), we find the pulsating traveling front equation:

$$-c\partial_y\phi-\partial_x(A(x)\partial_x\phi)-\partial_y(A(x)\partial_y\phi)-\partial_x(A(x)\partial_y\phi)-\partial_y(A(x)\partial_x\phi)\\ +q(x)\partial_y\phi+q(x)\partial_x\phi=g(\phi). \quad (3.4)$$

Proposition 1.1 in [32] gives the tail shape of $\phi(y,x)$ as follows.

PROPOSITION 3.1. *If (ϕ,c) is a classical solution of (3.4) and $g(u)$ is of the combustion type, then $\phi(y,x)$ is monotonically decreasing in y and there exists y_θ satisfying $\phi(y_\theta,x)\le\theta$, $\forall x$ (θ is as in (2.1)). When $y>y_\theta$, there exists $\lambda>0$ such that*

$$\phi(y,x)=e^{-\lambda y}\Phi(x),\quad y\ge y_\theta,\quad \Phi(x)\in C^2,\quad \Phi(x+L)=\Phi(x)>0. \quad (3.5)$$

Starting from a pulsating traveling front in (1.1), the front profile $u(x,t)$ for fixed t is the same as $\phi(y,x)$ for some given t. Thanks to (2.5), so is the front shape of $v(s,t)$. Therefore, given t, when $s>y_\theta+ct-\int_0^t\sigma(\tau)\,d\tau$, the tail shape of $v(s,t)$ is

$$v(s,t)=u(x,t)=\phi(x-ct,x)=\phi(s+\int_0^t\sigma(\tau)\,d\tau-ct,x)=e^{-\lambda(s+\int_0^t\sigma(\tau)\,d\tau-ct)}\tilde{\Phi}(s), \quad (3.6)$$

where $\tilde{\Phi}(s)=\Phi(x)\in C^2$ is positive and satisfies $\tilde{\Phi}(s+L)=\tilde{\Phi}(s)$.

The following theorem indicates that the front position of (3.2) is confined in a certain interval.

THEOREM 3.2. *Assume that $v(s,t)$ is positive, monotonically deceasing in s, $\int_0^{+\infty} v(s,t)\,ds$ is finite and $\sigma(t)>0$, $\forall t>0$. When $f(x,v)=g(v)$ in the new system (3.2) is of combustion type, starting from a pulsating traveling front, the value of $\int_0^{+\infty} v(s,t)\,ds$ has uniform lower and upper bounds that are independent of t.*

Proof. By integrating the equation for v in (3.2) from 0 to $+\infty$ and using the equation for $\sigma(t)$, we obtain the mass conservation equation on $[0,+\infty)$ such that

$$\int_0^{+\infty}\partial_t v\,ds+\sigma(t)(v(0,t)-\epsilon)=0. \quad (3.7)$$

We control $v(0,t)$ by $\int_0^\infty v\,ds$, then use (3.7) to find the uniform upper and lower bounds for $\int_0^{+\infty} v(s,t)\,ds$. The details are as follows.

Letting $s_\theta = y_\theta + ct - \int_0^t \sigma(\tau)\,d\tau$, from (3.6) we have $v(s_\theta,t) = e^{-\lambda y_\theta}\tilde{\Phi}(s_\theta) \le \theta$. Since $\tilde{\Phi}(s)$ in (3.6) is periodic in s, it has uniform upper and lower bounds for all s. There exist C_0, C_1 independent of t that satisfy

$$C_1 < \frac{\min_s \tilde{\Phi}}{\lambda} e^{-\lambda y_\theta} < \int_{s_\theta}^{+\infty} v(s,t)\,ds = \int_{s_\theta}^{+\infty} e^{-\lambda(s+\int_0^t \sigma(\tau)\,d\tau - ct)}\tilde{\Phi}(s)\,ds$$
$$< \frac{\max_s \tilde{\Phi}}{\lambda} e^{-\lambda y_\theta} < C_0. \tag{3.8}$$

If $s_\theta > 0$, then

$$\int_0^{+\infty} v(s,t)\,ds < s_\theta v(0,t) + \int_{s_\theta}^{+\infty} v(s,t)ds < s_\theta v(0,t) + C_0.$$

Therefore, the positivity of $\sigma(t)$ and (3.7) give

$$\partial_t \int_0^{+\infty} v(s,t)\,ds < -\sigma(t)\Big(\frac{1}{s_\theta}\int_0^{+\infty} v(s,t)\,ds - \frac{C_0}{s_\theta} - \epsilon\Big). \tag{3.9}$$

Using Gronwall's inequality, we have the existence of an upper bound for $\int_0^{+\infty} v(s,t)\,ds$ that is independent of t. Otherwise when $s_\theta \le 0$, the upper bound is $\int_0^{+\infty} v(s,t)\,ds \le \int_{s_\theta}^{+\infty} v(s,t)\,ds < C_0$.

For the uniform lower bound, when $s_\theta \ge 0$, due to the positivity of $v(s,t)$ in s, we have $\int_0^{+\infty} v(s,t)\,ds \ge \int_{s_\theta}^{+\infty} v(s,t)\,ds > C_1$. When $s_\theta < 0$, from (3.6), we have

$$v(0,t) = e^{-\lambda(\int_0^t \sigma(\tau)\,d\tau - ct)}\tilde{\Phi}(0)$$
$$< \frac{\max_s \tilde{\Phi}(s)}{\lambda \min_s \tilde{\Phi}(s)} \int_0^{+\infty} e^{-\lambda(s+\int_0^t \sigma(\tau)\,d\tau - ct)}\tilde{\Phi}(s)\,ds = C_2 \int_0^{+\infty} v(s,t)\,ds.$$

Then the positivity of $\sigma(t)$ and (3.7) gives

$$\partial_t \int_0^{+\infty} v(s,t)\,ds > -\sigma(t)\Big(C_2 \int_0^{+\infty} v(s,t)\,ds - \epsilon\Big).$$

We can use Gronwall's inequality again to get the uniform lower bound. ∎

The boundary conditions

For general reaction terms, the pulsating front connects two steady states: one is 0 at $+\infty$, and the other may remain not explicitly known.

If we define the steady state of (1.1) by $p(y,x)$, which satisfies (3.4) with $c=0$, then since $y=x$, $p(y,x)$ only depends on x such that $p(y,x) \equiv \bar{p}(x)$. When $c=0$, (3.4) becomes

$$-\partial_x(A(x)\partial_x \bar{p}) + q(x)\partial_x \bar{p} = f(x,\bar{p}). \tag{3.10}$$

$\bar{p}(x)$ is the limiting state of $u(x,t)$ when $x \to -\infty$ and satisfies $\bar{p}(x+L) = \bar{p}(x)$. Therefore, we can use a more general boundary condition $u(x_l) = u(x_l + L)$ instead of

$u(x_l)=1$. Letting $x_l=s_l+\int_0^t\sigma(\tau)d\tau$, then from (2.5), we can find the boundary condition for v at s_l that is equivalent to $u(x_l+L)=u(x_l)$ such that

$$v(s_l)=v(s_l+L).$$

The other boundary condition is $v(s_r)=0$.

REMARK 3.3. The steady state of (1.1) is defined by $p(y,x)$, which satisfies (3.4) with $c=0$. This is different from the usual definition $\partial_t u=0$, although for both definitions the steady states are the same and satisfy (3.10). We use this statement because it is also consistent with the steady state definition for the time periodic case. We will see in Section 4 that the steady states of the time periodic advection diffusion reaction equation depend on time. The usual definition $\partial_t u=0$ is no longer applicable.

The choices of $\mathfrak{P}$

As we have claimed, the specific choice of $\mathfrak{P}(v^B)$ in (3.3) is due to the positivity of c. Similar to the traveling wave simulations in [27], we should choose different $\mathfrak{P}$ for different signs of c such that

$$\mathfrak{P}(v^B)=\begin{cases}\mathfrak{P}_r(v^B), & \text{if } c>0,\\ \mathfrak{P}_l(v^B), & \text{if } c<0,\end{cases} \tag{3.11}$$

where

$$\mathfrak{P}_r(v^B)=\frac{1}{\epsilon}\Big(A(x)\partial_s v^B|_0^{s_r}-\int_0^{s_r}q(x)\partial_s v^B\,ds+\int_0^{s_r}f(x,v^B(s,t))\,ds\Big), \tag{3.12}$$

$$\mathfrak{P}_l(v^B)=\frac{1}{v(s_l)-\epsilon}\Big(A(x)\partial_s v^B|_{s_l}^0-\int_{s_l}^0q(x)\partial_s v^B\,ds+\int_{s_l}^0f(x,v^B(s,t))\,ds\Big). \tag{3.13}$$

If $c=0$, both $\mathfrak{P}_r$ and $\mathfrak{P}_l$ can be employed, which is similar to obtaining the steady state solution in the traveling wave simulations in [27]. If the sign of c is not known a priori, to achieve front position confinement, numerically we need to try both $\mathfrak{P}_r$, $\mathfrak{P}_l$. However, in most problems under consideration, it is not difficult to determine the sign of c by looking at the propagation direction of the original time evolution equation.

This different choice of $\mathfrak{P}$ for different sign of c is necessary. Though we are not able to prove rigorously the convergence of (2.3) to a periodic pattern in t (with $\mathfrak{P}$ as in (3.11)), the necessity can be seen roughly by the discussion of the effect of ϵ. When we try to find the uniform upper and lower bounds for $\int_0^{+\infty}v(s,t)\,ds$, Gronwall's inequality is employed. If $\sigma(t)<0$ in (3.9), we can no longer find a uniform upper bound, but a bound that is exponentially increasing in t. Therefore, the front position is not confined if we keep using (3.3) for $\sigma(t)<0$.

By integrating the equation for v in (3.3) from s_l to 0 and using $\sigma(t)=\mathfrak{P}_l(v^B)$, we obtain the following mass conservation equation on $[s_l,0]$:

$$\int_{s_l}^0\partial_t v^B\,ds-\sigma^B(t)(v^B(0,t)-\epsilon)=0. \tag{3.14}$$

Comparing with (3.7), we see that the sign in front of $\sigma(t)$ is different. When $\sigma(t)<0$, if we want to use an inequality similar to (3.9) to confine the front position by an upper bound of $\int_{s_l}^0 v\,ds$, (3.14) gives the correct sign after using Gronwall's inequality.

Moreover, notice that the traveling wave solution is a special case of the pulsating traveling front. In [27], the authors have shown the necessity of different choices of $\mathfrak{P}$ in the traveling wave simulations; subsequently, it is also necessary in the more general case discussed here.

In summary, we are going to solve the new parabolic system

$$\begin{cases} \partial_t v^B - \sigma^B(t)\partial_s v^B - \partial_s(A(x)\partial_s v^B) + q(x)\partial_s v^B = f(x,v^B), \quad s\in[x_l,x_r], \\ \sigma^B(t) = \mathfrak{P}(v^B), \\ x = s + \int_0^t \sigma^B(\tau)\,d\tau, \\ v^B(s_l,t) = v^B(s_l+L,t), \qquad v^B(s_r,t) = 0, \end{cases} \tag{3.15}$$

with $\mathfrak{P}(v^B)$ as in (3.11).

3.2. Scheme discretizations. We use a uniform mesh such that

$$\Delta s = \frac{s_r - s_l}{N_1+N_2} = \frac{s_r}{N_2} = -\frac{s_l}{N_1}; \qquad s_j = j\Delta s, \quad \text{for } j = -N_1,\cdots,0,\cdots N_2.$$

Let the time steps be $n\Delta t$, $n=0,1,\cdots$. Assuming that v^{Bn} is known, we consider the discretizations of (3.3). To allow the space and time steps to be of the same order, as well as achieve stability and use a linear solver, we treat the diffusion term implicitly and reaction term explicitly, whereas two different discretizations are proposed for the advection term.

To maintain scheme stability even when discontinuous or sharp fronts occur, we have to use shock capturing methods for the addition term. However, even for the original advection diffusion reaction equation, the additional numerical diffusion introduced by the shock capturing methods will accelerate the front speeds. In our new system (3.3), this makes the error of $x = s + \int_0^t \sigma(\tau)\,d\tau$ increase linearly with time. As time goes on, the linearly increasing error in x breaks down the convergence of σ^B. On the other hand, a centered finite difference method for advection introduces no numerical diffusions in space but cannot treat discontinuous or sharp fronts. As discussed in [13], since the advection term is linear, starting from smooth initial data and using small enough mesh size, an implicit centered finite difference method gives a positive, stable solution.

We will compare the results of the upwind method and the centered finite difference method to understand the influence of numerical diffusion. We present here the details of both discretizations.

Upwind method: When $A(x)=0$ or $|A(x)|$ is very small, discontinuities or sharp fronts can appear in the solutions. Thus we have to use shock capturing methods

for the advection term. The simplest first order upwind method for (3.3) is

$$\begin{cases} \frac{v_j^{Bn+1}-v_j^{Bn}}{\Delta t}-\big(\sigma^{Bn+1}-q(x_j^n)\big)D_{Fj}(v^{Bn})-D_{j+}(A(x_{j-1/2}^n)D_{j-}v^{Bn+1})=f(x_j^n,v_j^{Bn}), \\ \qquad\qquad\qquad\qquad\qquad\qquad\qquad\qquad\qquad\qquad\qquad\qquad j=-N_1+1,\cdots,0,\cdots,N_2-1, \\ \sigma^{Bn+1}=\frac{1}{\epsilon}\Big(\big(A(x_{N_2-1/2}^n)\frac{v_{N_2}^{Bn+1}-v_{N_2-1}^{Bn+1}}{\Delta s}-A(x_{-1/2}^n)\frac{v_0^{Bn+1}-v_{-1}^{Bn+1}}{\Delta s}\big) \\ \qquad\qquad\qquad\qquad -\Sigma_{i=0}^{N_2-1}q(x_i^n)D_{Fi}(v^{Bn})\Delta s+\Sigma_{i=0}^{N_2-1}f(x_i^n,v_i^{Bn})\Delta s\Big), \\ x_j^{n+1}=s_j+\frac{\Delta t}{2}\Sigma_{i=0}^{n+1}(\sigma^{Bi}+\sigma^{Bi+1}), \qquad x_{j-1/2}^{n+1}=\frac{x_j^{n+1}+x_{j-1}^{n+1}}{2}, \\ v_{-N_1}^{Bn+1}=1, \qquad v_{N_2}^{Bn+1}=0. \end{cases} \tag{3.16}$$

Here $D_{j-}v^B=\frac{v_j^B-v_{j-1}^B}{\Delta s}$, and $D_{j+}v^B=\frac{v_{j+1}^B-v_j^B}{\Delta s}$. $D_F(v^{Bn})$ indicates the flux difference divided by Δs, i.e.

$$D_{Fj}(v^{Bn})=\frac{F_{j+\frac{1}{2}}(v^{Bn})-F_{j-\frac{1}{2}}(v^{Bn})}{\Delta s}, \tag{3.17}$$

with $F_{j\pm\frac{1}{2}}$ the numerical fluxes of some hyperbolic solver. Specifically, for the upwind finite difference method, $F_{j\pm\frac{1}{2}}$ depends on the sign of $-(\sigma-q(x_{j\pm\frac{1}{2}}^n))$ such that

$$F_{j+\frac{1}{2}}=\begin{cases} v_{j+1}^{Bn}, & \text{if } -(\sigma-q(x_j^n))<0, \\ v_j^{Bn}, & \text{if } -(\sigma-q(x_j^n))>0. \end{cases}$$

If we multiply the equations for $v_0^{Bn+1},v_1^{Bn+1},\cdots,v_{N_2-1}^{Bn+1}$ in (3.16) by Δs and sum them up, comparing with the equation for σ^{Bn+1} in (3.16), we find the discrete mass conservation equation on $[0,s_r]$:

$$\sum_{j=0}^{N_2-1}\frac{\Delta s}{\Delta t}(v_j^{Bn+1}-v_j^{Bn})-\sigma^{Bn}\big(F_{N_2-\frac{1}{2}}(v^{Bn})-F_{-\frac{1}{2}}(v^{Bn})\big)=\epsilon\sigma^{Bn+1}. \tag{3.18}$$

If v^{Bn} has no jump near 0 and x_r, then $F_{-\frac{1}{2}}(v^{Bn})\approx v^B(0)$ and $F_{N_2-\frac{1}{2}}(v^{Bn})\approx v^B(x_r)$. Assuming enough regularity, (3.18) is a discretization of (3.7).

Centered finite difference method: As in [3, 19], the analysis of a pulsating traveling front is always carried out when $|A(x)|>r>0$, i.e. when $|A(x)|$ has a lower bound that is not negligible. In this case the solutions are always smooth and we can use implicit centered finite difference method:

$$\begin{cases} \frac{v_j^{Bn+1}-v_j^{Bn}}{\Delta t}-\big(\sigma^{Bn}-q(x_j^n)\big)\frac{v_{j+1}^{Bn+1}-v_{j-1}^{Bn+1}}{2\Delta s}-D_{j+}(A(x_{j-\frac{1}{2}}^n)D_{j-}v^{Bn+1})=f(x_j^n,v_j^{Bn}), \\ \qquad\qquad\qquad\qquad\qquad\qquad\qquad\qquad\qquad\qquad\qquad\qquad j=-N_1+1,\cdots,0,\cdots,N_2-1, \\ \sigma^{Bn+1}=\frac{1}{\epsilon}\Big(\big(A(x_{N_2-1/2}^n)\frac{v_{N_2}^{Bn+1}-v_{N_2-1}^{Bn+1}}{\Delta s}-A(x_{-1/2}^n)\frac{v_0^{Bn+1}-v_{-1}^{Bn+1}}{\Delta s}\big) \\ \qquad\qquad -\Sigma_{i=0}^{N_2-1}q(x_i^n)\frac{v_{i+1}^{Bn+1}-v_{i-1}^{Bn+1}}{2}+\Delta s\Sigma_{i=0}^{N_2-1}f(x_i^n,v_i^{Bn})\Big), \\ x_j^{n+1}=s_j+\frac{\Delta t}{2}\Sigma_{i=0}^{n}(\sigma^{i}+\sigma^{i+1}), \qquad x_{j-1/2}^{n+1}=\frac{x_j^{n+1}+x_{j-1}^{n+1}}{2}, \\ v_{-N_1}^{Bn+1}=1, \qquad v_{N_2}^{Bn+1}=0. \end{cases} \tag{3.19}$$

Here $D_{j-}v^B$, and $D_{j+}v^B$ are the same as in the upwind method. Multiplying the equations for $v_0^{Bn+1}, v_1^{Bn+1}, \cdots, v_{N_2-1}^{Bn+1}$ in (3.19) by Δs, summing them up, and using the equation for σ^{Bn+1} in (3.19), we obtain again the discrete mass conservation equation:

$$\sum_{j=0}^{N_2-1} \frac{\Delta s}{\Delta t}(v_j^{Bn+1} - v_j^{Bn}) + \frac{\sigma^{Bn}}{2}(v_{-1}^{Bn+1} + v_0^{Bn+1} - v_{N_2-1}^{Bn+1}) = \epsilon\sigma^{Bn+1}.$$

Assuming enough regularity, this is a consistent discretization of (3.7).

REMARK 3.4. According to [13], the centered finite difference method for $\partial_t u + a\partial_s u = d\partial_{ss} u$, such that

$$\partial_t u_j = \frac{a}{2\Delta s}(u_{j-1} - u_{j+1}) + \frac{d}{\Delta s^2}(u_{j-1} - 2u_j + u_{j+1}),$$

is positive when $|a\Delta s/d| \le 2$. Additionally, if fully implicit time discretization is employed, Von Neumann stability analysis gives unconditional stability. In our problem, the coefficients are no longer constants but depend on x, however, thanks to $A(x) > \gamma$ and the smoothness of the solution, we can expect that the centered finite difference method is stable and non-oscillating when the mesh size is small enough.

REMARK 3.5. Due to the numerical diffusion, the front position recovered from the upwind method will be ahead of the exact solution. This phenomenon has already been noticed in the simulations of the advection reaction equation [16]. The numerical diffusion increases the propagation speed. Some authors try to design well balanced schemes to avoid this problem. However, most of them can only balance the steady states [15, 23]. The strategy of designing well balanced schemes that can capture the correct front position at all times is out of the scope of this present paper. Though the front position is not correct when t becomes large, L^1 convergence of the front position is numerically observed.

4. Time periodic case

4.1. The new parabolic system. For the time periodic advection diffusion reaction equation (2.4), we have to specify $\mathfrak{P}(v)$ and truncate it in a bounded domain $[s_l, s_r]$. The new parabolic system is

$$\begin{cases} \partial_t v^B - \sigma^B(t)\partial_s v^B - \partial_s(A(t)\partial_s v^B) + q(t)\partial_s v^B = f(t, v^B), \quad s \in [s_l, s_r], \\ \sigma^B(t) = \begin{cases} \frac{1}{\epsilon}\Big(A(t)\partial_s v^B|_0^{s_r} - q(t)v^B|_0^{s_r} + \int_0^{s_r} f(t, v^B(s,t))\,ds\Big), & c > 0, \\ \frac{1}{v(s_l)-\epsilon}\Big(A(t)\partial_s v^B|_{s_l}^0 - q(t)v^B|_{s_l}^0 + \int_{s_l}^0 f(t, v^B(s,t))\,ds\Big), & c < 0. \end{cases} \end{cases} \tag{4.1}$$

Formally, (4.1) is close to the space periodic system (3.15), and we can explain the effect of ϵ and the necessity of different choices of $\mathfrak{P}$ in a similar way as for (3.15). The boundary conditions for the time periodic case are simpler than the space periodic case.

Boundary conditions

In order to determine the boundary conditions for system (4.1), we have to find the two connected limiting states. We may assume that one of two limiting states is a positive steady state, defined as in Remark 3.3, while the other one is zero. In many cases under study, they are $u(x) \equiv$ constant and $u(x) \equiv 0$. For the bistable reaction,

[28, 29] considered a space-uniform steady state that changes periodically in time. We explain in the subsequent part that the steady state is also space-uniform for some other types of reaction.

The time periodic pulsating traveling front has the form

$$u(x,t)=\phi(x-ct,t)\equiv\phi(y,t),\quad y=x-ct\in\mathbb{R},$$

where $\phi(y,t)$ is periodic in t. Then by substituting $\phi(y,t)$ into (1.3), the pulsating traveling front equation is

$$\partial_t\phi-c\partial_y\phi-\partial_y(A(t)\partial_y\phi)+q(t)\partial_y\phi=f(t,\phi). \tag{4.2}$$

When $y\to-\infty$, the limiting state $p(y,t)>0$ satisfies

$$\begin{cases}\partial_t p-\partial_y(A(t)\partial_y p)+q(t)\partial_y p=f(t,p),\\ \text{periodic in both } y \text{ and } t.\end{cases} \tag{4.3}$$

The existence and uniqueness of a rigorously positive $p(y,t)$ has been proved in [19], under some regularity conditions for $f(t,p)$ and when

$$\begin{aligned}&f(t,0)\equiv 0,\qquad \lim_{r\to 0+} f(t,r)/r>0,\\ &\forall t\in\mathbb{R},\ r\to f(t,r)/r \text{ is decreasing in } r>0,\\ &\exists M>0 \text{ such that } \forall r\ge M,\ f(t,r)\le 0.\end{aligned}$$

Additionally, let $\hat{p}(t)>0$ be the solution to $\partial_t\hat{p}=f(t,\hat{p})$. Since $\hat{p}(t)$ is periodic in t and homogeneous in y, $p(y,t)=\hat{p}(t)$ satisfies (4.3). We know from the uniqueness of positive solutions to (4.3) that $p(y,t)=\hat{p}(t)$ is the only possible limiting state.

We are not able to prove rigorously, for general f, that the solution of (4.3) is homogeneous in y. However, this is true for most applications under consideration. Therefore, numerically, we can use the following boundary conditions:

$$\partial_s v^B(s_l)=0,\qquad v^B(s_r)=0.$$

4.2. Details of the discretization. As in Section 3.2, we compare two different space discretizations: one uses the upwind method for the advection term while the other uses the centered finite difference method. Let all the notations be the same as in Section 3.2. Then the schemes can be written as follows:

The upwind method:

$$\begin{cases}\frac{v_j^{Bn+1}-v_j^{Bn}}{\Delta t}-(\sigma^{Bn}-q(t^n))D_{Fj}(v^{Bn})-A(t^n)D_{j+}D_{j-}v^{Bn+1}=(f(t^n,v_j^{Bn}))\\ \qquad\qquad\qquad\qquad\qquad\qquad\qquad\qquad\qquad\qquad j=-N_1+1,\cdots,0,\cdots,N_2-1,\\ \sigma^{Bn+1}=\frac{1}{\epsilon}\Big(\big(A(t^n)\frac{v_{N_2}^{Bn+1}-v_{N_2-1}^{Bn+1}}{\Delta s}-A(t^n)\frac{v_0^{Bn+1}-v_{-1}^{Bn+1}}{\Delta s}\big)\\ \qquad\qquad -q(t^n)\Delta s\Sigma_{i=0}^{N_2-1}D_{Fi}(v^{Bn})+\Delta s\Sigma_{i=0}^{N_2-1}f(t^n,v_i^{Bn})\Big),\\ \frac{v_{-N_1}^{Bn+1}-v_{-N_1+1}^{Bn+1}}{\Delta x}=0,\qquad v_{N_2}^{Bn+1}=0.\end{cases} \tag{4.4}$$

with

$$D_{Fj}=\begin{cases}\frac{1}{\Delta s}\big(v_j^{Bn}-v_{j-1}^{Bn}\big), & \text{if } -(\sigma^{Bn}-q(t^n))>0,\\ \frac{1}{\Delta s}\big(v_{j+1}^{Bn}-v_j^{Bn}\big), & \text{if } -(\sigma^{Bn}-q(t^n))<0.\end{cases}$$

The centered finite difference method:

$$\begin{cases} \frac{v_j^{Bn+1}-v_j^{Bn}}{\Delta t}-(\sigma^{Bn}-q(t^n))\frac{v_{j+1}^{Bn+1}-v_{j-1}^{Bn+1}}{2\Delta s}-A(t^n)D_{j+}D_{j-}v^{Bn+1}=(f(t^n,v_j^{Bn})), \\ \qquad\qquad\qquad\qquad\qquad\qquad\qquad\qquad\qquad\qquad j=-N_1+1,\cdots,0,\cdots,N_2-1, \\ \sigma^{Bn+1}=\frac{1}{\epsilon}\Big(\big(A(t^n)\frac{v_{N_2}^{Bn+1}-v_{N_2-1}^{Bn+1}}{\Delta s}-A(t^n)\frac{v_0^{Bn+1}-v_{-1}^{Bn+1}}{\Delta s}\big) \\ \qquad\qquad -\frac{q(t^n)}{2}\big(v_{N_2}^{Bn+1}+v_{N_2-1}^{Bn+1}-v_0^{Bn+1}-v_{-1}^{Bn+1}\big)+\Delta s\Sigma_{i=0}^{N_2-1}(f(t^n,v_i^{Bn}))\Big), \\ \frac{v_{-N_1}^{Bn+1}-v_{-N_1+1}^{Bn+1}}{\Delta s}=0, \qquad v_{N_2}^{Bn+1}=0. \end{cases} \tag{4.5}$$

When $\gamma<A(t)<\Gamma$ with γ, Γ two positive constants, according to Remark 3.4, we can use small enough Δs to guarantee the stability and positivity of the centered finite difference method. Other higher order shock capturing methods can be employed when sharp fronts occur.

5. Numerical examples

In this section, to show the performance of the proposed scheme and illustrate its ability to find the front velocity, three numerical examples are presented: two for the space periodic case and one for the time periodic case.

We consider the time interval $[0,t]$ and use the uniform time step $\Delta t=t/M$ with M some integer. If the solution of (1.1) or (1.3) converges to a pulsating traveling front, then L_σ, T_σ, and c_σ in (2.6) should converge to constants. According to the choice of $\mathfrak{P}$ in (3.11), different values of ϵ give different $\sigma(t)$, whereas the periods T, L and front velocity c are determined by the original equation and not by the specific parameter that we use. This is because the time evolution of $\sigma^B(t)$ itself has no physical meaning, while its periods do. Therefore, although L, T, and c are found by $\sigma(t)$ through (2.6) in our method, we have to numerically verify the independence of T, L, and c on ϵ.

Assume $(v^B(s,t),\sigma^B(t))$ has converged to a periodic pattern in t. If $\sigma^M>\sigma^{M-1}$ (M is the total number of time steps) are away from each other, then the periods T_σ, L_σ and the corresponding front velocity c_σ can be obtained numerically as follows: (1) Find from $\{1,\cdots,M\}$ all the m which satisfy $\sigma^m>\sigma^M$, $\sigma^{m-1}\le\sigma^M$, and let them be $m_1,m_2,\cdots,m_n$. (2) For $j=2,\cdots,n$, the numerical period $T_{\sigma j}$ are given by $\Delta t(m_j-m_{j-1})$. (3) Calculate $L_{\sigma j}=\sum_{l=m_{j-1}}^{m_j-1}\Delta t(\sigma_m+\sigma_{m+1})/2$, which is the discrete approximation of $\int_{m_{j-1}\Delta t}^{m_j\Delta t}\sigma(\tau)d\tau$. (4) From the definition in (2.6), the $c_{\sigma j}$ are given by $\frac{L_{\sigma j}}{T_{\sigma j}}$. When $\sigma^M<\sigma^{M-1}$, a similar procedure using a sequence of σ^m that satisfy $\sigma^m<\sigma^M$, $\sigma^{m-1}>\sigma^M$ can be used.

Example 1: Let

$$A(x)=1+0.8*sin(2\pi x), \quad q(x)=0.5*cos(2\pi x), \qquad \text{for } x\in[0,1],$$

and then extend them to the whole real line. The space period is $L=1$ in this example. We consider the combustion reaction case:

$$f(x,u)=20u_\theta(1-u), \qquad \theta=10^{-2}, \tag{5.1}$$

where $u_\theta=0$ for $u\le\theta$ and $u_\theta=u-\theta$ for $u>\theta$. The two steady states $u\equiv1$ and $u\equiv0$ are uniform and, heuristically, $u\equiv1$ invades $u\equiv0$ in a periodic manner. Starting from

a continuous function

$$v^{B0} = \begin{cases} 1, & s \in [s_l, -5], \\ \frac{e^{-(s+5)^2} - e^{-100}}{1 - e^{-100}}, & s \in [-5, 5], \\ 0, & s \in [5, s_r], \end{cases}$$

which is consistent with the boundary conditions in (3.3), the performances of (3.16) and (3.19) are tested in the following aspects:

i) Comparison with direct time evolutionary simulation;
ii) The convergence with respect to the mesh size;
iii) The convergence with respect to the time step;
iv) The effect of different choices of ϵ;
v) The effect of different choices of computational domain $[s_l, s_r]$.

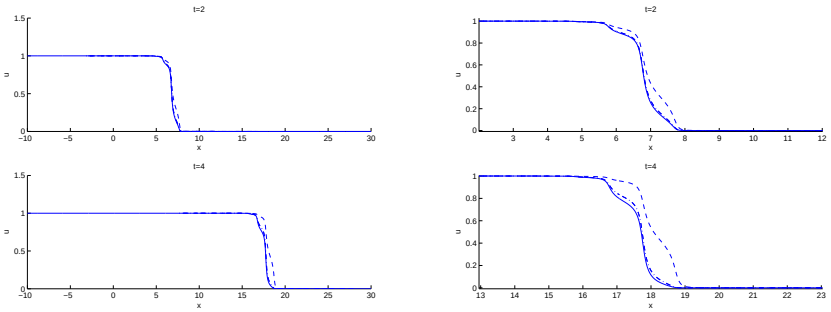

FIG. 5.1. *Example 1 of space periodic pulsating front. To compare our scheme with the direct time evolutionary simulation, we show the results of the direct time evolutionary simulation* $\tilde{u}^B$ *(solid lines) when* $t=2$ *(top) and* $t=4$ *(bottom), and the* u^B *recovered from the upwind method (dashed lines) and the centered difference method (dash dotted lines) . Here we use* $\Delta s = 1/100$, $\Delta t = 1/2000$ *and* $\epsilon = 0.5$. *The right figure is the zoom in of the one on the left.*

i) Comparison with direct time evolutionary simulation: We have claimed in previous discussions that our scheme can recover u at the continuous level. Here we show that, at the discrete level, the u^B that is recovered from the solution of (3.16), by shifting $\int_0^t \sigma(\tau)d\tau$ in s and extending both sides by the steady state solutions (1 and 0), is the same as the $\tilde{u}^B$ that is obtained from direct time evolutionary simulation. The direct time evolutionary simulations are implemented by letting $\sigma^{Bn} = 0$ in (3.16) and using a larger computational domain. Here we have used $[x_l, x_r] = [-10, 30]$, $\Delta s = 1/100$, and $\Delta t = 1/2000$ for the direct time evolutionary simulations and $[s_l, s_r] = [-10, 10]$, $\epsilon = 0.5, \Delta s = 1/100$, and $\Delta t = 1/2000$ for our relaxation scheme. The shifting is done by replacing s_j in $v^B_{\Delta s, \Delta t}(s_j, t)$ by $x_j = s_j + \frac{\Delta t}{2}\sum_{i=0}^{n}(\sigma^i + \sigma^{i+1})$, which involve no interpolation. As shown in figure 5.1, numerically, the front positions of $\tilde{u}^B$ and u^B seem different for fixed t. The difference between $\tilde{u}^B$ and u^B increases with time. However, as we will see in ii), if we refine the mesh then the difference decreases to zero, which verifies that $\tilde{u}^B$ can be recovered from v^B at the continuous level.

These numerical front displacements are unavoidable for almost all advection diffusion reaction equation long time simulations. This is due to the numerical diffusion and can be reduced when using higher order methods and finer meshes. To control

the front displacements is not the topic of this present paper, but we can see that the centered finite difference method with no numerical diffusion is more accurate than the upwind method.

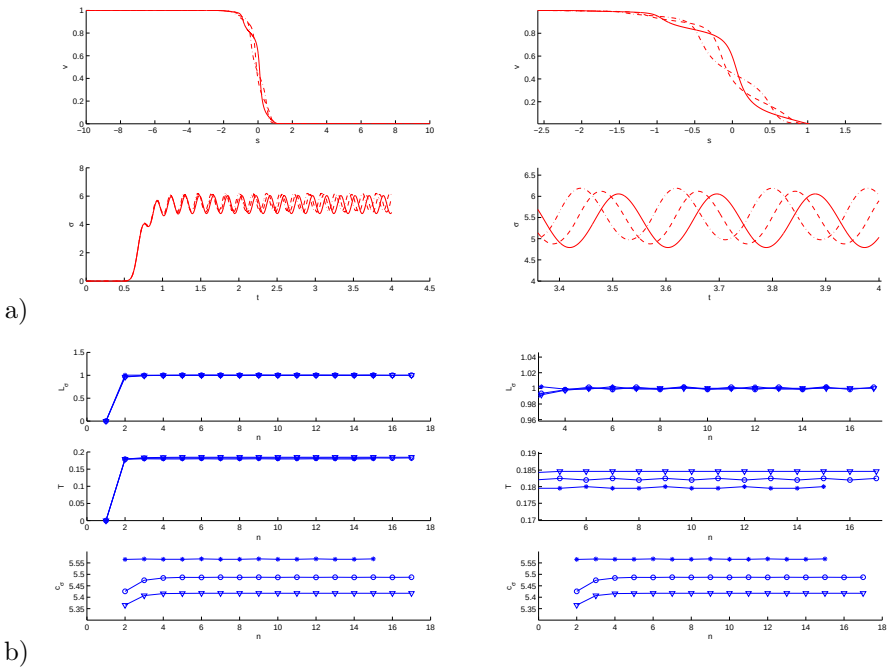

FIG. 5.2. *Example 1. The numerical results of the upwind method using* $[s_l, s_r] = [-10, 10]$, $\Delta t = 1/2000$, $\epsilon = 0.5$, *and different* Δs *are presented. a): Top subplot gives the front shape* v^B *at time* $t = 4$ *while the bottom subplot depicts the time evolution of* σ^B. *The dash dotted, dashed, and solid lines are respectively the numerical results of* $\Delta s = 1/100$, $\Delta s = 1/200$, *and the "exact" solution. The right two subplots are the amplification of the left two subplots; b): The numerical* L_σ *(top),* T_σ *(middle), and* c_σ *(bottom) for each* $\sigma^n \in [\sigma^{M-1}, \sigma^M]$ *as discussed in the third paragraph of this section. The stars, circles, and triangles are the results of* $\Delta s = 1/100$, $\Delta s = 1/200$, *and the "exact" solution, respectively. The right three subplots are the amplification of the left three subplots.*

ii) The convergence with respect to space: We investigate the convergence with respect to space by comparing the upwind method (3.16) and centered finite difference method (3.19).

From figures 5.2 and 5.3 for given Δs, Δt, we can see that $\sigma(t)$ converges to a periodic patten, and the numerical T_σ, L_σ, and c_σ converge to constants. Moreover, the constant to which L_σ converges is close to 1, which is the same as the period of the coefficients.

Denote the numerical solutions of Δs and Δt by $v^B_{\Delta x, \Delta t}(s_i, t_j)$ and $\sigma^B_{\Delta s, \Delta t}(t_j)$, where (s_i, t_j) are the discrete nodes. In figure 5.2, the numerical results of the upwind method calculated with $\Delta t = 1/2000$ and different Δs are presented. We can see that the $\sigma^B_{\Delta s, \Delta t}(t_j)$ are initially close together, but afterwards, although the $\sigma^B_{\Delta s, \Delta t}(t)$ evolve in a similar periodic manner, the periods change with Δs, which makes $\sigma^B_{\Delta s, \Delta t}(t_j)$ away from each other when t_j becomes big. The numerical displacements of the periods of $\sigma^B(t)$ are due to the numerical diffusions and the linearly increasing error in $\int_0^t \sigma(\tau) d\tau$, which can be improved by using higher order discretizations. As we can see from figure 5.3, the second order centered finite difference method

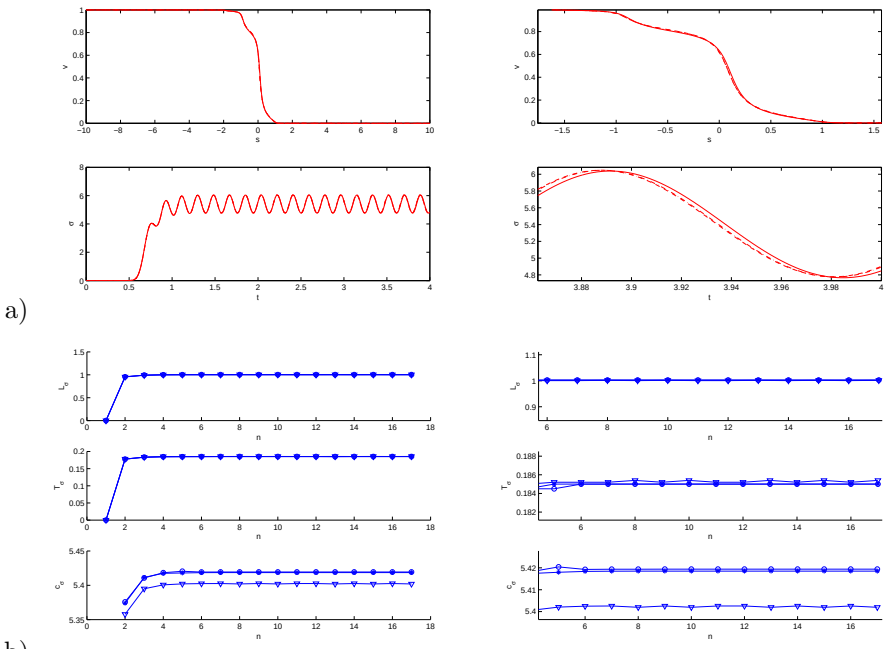

FIG. 5.3. *Example 1. The numerical results of the centered finite difference method using* $[s_l, s_r] = [-10, 10]$, $\Delta t = 1/2000$, $\epsilon = 0.5$, *and different* Δs *are presented. a): Top subplot gives the front shape* v^B *at time* $t = 4$ *while the bottom subplot depicts the time evolution of* σ^B. *The dash dotted, dashed, and solid lines are respectively the numerical results of* $\Delta s = 1/100$, $\Delta s = 1/200$, *and the "exact" solution. The right two subplots are the amplification of the left two subplots. b): The numerical* L_σ *(top),* T_σ *(middle), and* c_σ *(bottom) for each period. The stars, circles, and triangles are the results of* $\Delta s = 1/100$, $\Delta s = 1/200$, *and the "exact" solution, respectively. The right three subplots are the amplification of the left three subplots.*

significantly improves this displacement.

For the upwind method, although there are period variations in $\sigma(t)$, we can find the space convergence for the constants to which L_σ, T_σ, and c_σ converge. Additionally, at a fixed time, different Δs give different front shapes, but $u^B(x_j,t)$ (recovered from $v^B(s_j,t)$) exhibits first order convergence in the L^1 norm. In table 5.1, we compare the numerical results of different Δx at a fixed time $t = 4$. The "exact" solution (v^B, σ^B) is given by a centered finite difference method with a very fine mesh $\Delta s = 1/800$, $\Delta t = 1/5000$. E_{up}, E_{ct} are the discrete L^1 norms of the difference between $u^B_{\Delta s,\Delta t}$ and the "exact" solution u^B. The subscripts "up" and "ct" represent, respectively, the results of the upwind method and the centered finite difference method. More precisely, the discrete L^1 norm is

$$\frac{\sum_{i=-N_1}^{N_2} \left| u^B_{\Delta s,\Delta t}(x_i,t) - u^B(x_i,t) \right|}{N_1 + N_2 + 1}.$$

Here x_i is as in (3.16) and (3.19) when calculating $u^B_{\Delta s,\Delta t}(x_i,t)$, while the values of $u^B(x_i,t)$ are obtained by linear interpolation of the "exact" solution at x_i. We can see from table 5.1 and figure 5.4, which displays the log-log plot of the errors in table 5.1, the first order convergence of the upwind method and second order convergence of the centered finite difference method.

Δx	$\|E_{ct}\|_1$	c_{ct}	$\|E_{up}\|_1$	c_{up}
1/25	$2.70*10^{-3}$	6.0087	$1.09*10^{-1}$	6.0161
1/50	$6.35*10^{-4}$	5.3966	$5.26*10^{-2}$	5.7143
1/100	$1.06*10^{-4}$	5.4014	$2.55*10^{-2}$	5.5573
1/200	$3.67*10^{-5}$	5.4023	$1.23*10^{-2}$	5.4777

TABLE 5.1. *Example 1 of space periodic pulsating front. For different Δx, the numerical results of (3.16) and (3.19) with $[s_l, s_r] = [-10, 10]$, $\Delta t = 1/5000$, and $\epsilon = 0.5$ are presented. Here $\|E\|_1$ is the discrete L^1 norm and the subscripts "up" and "ct" respectively represent the results of the upwind method and the centered finite difference method.*

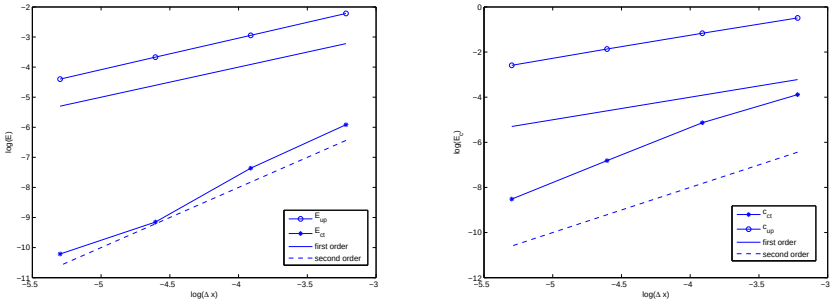

FIG. 5.4. *The log-log plot of the errors in table 5.1. The stars and circles are respectively the errors for the centered finite difference method and the upwind method. The dashed and solid lines give the slopes of second and first order convergence. Left: The errors of the traveling front, $\|E_up\|_1$, and $\|E_{ct}\|_1$. Right: The errors of the traveling velocity c_{ct} and c_{up}.*

iii) The convergence with respect to time: In figure 5.5, the numerical results of $\Delta s = 1/800$ and different Δt are presented. For different Δt, the $\sigma^B_{\Delta s, \Delta t}(t_j)$ are close to each other when t_j is small, but away from each other when t_j becomes big. Therefore, as for the spatial convergence, we consider the discrete L^1 norm of the difference between $u^B_{\Delta s, \Delta t}$ and u^B. L_σ, T_σ, and c_σ all converge to constants. For different Δt, the constants to which c_σ converges are displayed in table 5.2. Table 5.2 demonstrates the first order convergence in time for both the traveling front u^B and the front velocity c_σ.

In figure 5.5, the numerical results of the upwind method and the centered finite difference method seem identical. This is because our purpose here is to compare the effect of different time steps; small space steps are used and the numerical diffusion introduced by the two different space discretizations is small compared to the numerical diffusion introduced by the time discretization.

iv) The effect of ϵ: Since the original traveling front u and the traveling velocity c do not depend on ϵ, we test three different ϵ ($\epsilon = 0.01$, 0.1, and 0.5) to verify this independence. The evolutions of σ^B are presented in figure 5.6. For different ϵ, all $\sigma^B(t)$ become periodic as time goes on, but the profiles are different. $\sigma(t)$ itself has no physical meaning and is not unique, nevertheless, the same L_σ, T_σ, and c_σ can be obtained numerically. From figure 5.7, at both times $t = 1$, $t = 2$, different ϵ provide almost the same u^B, whether we arrive at the pulsating traveling front or not.

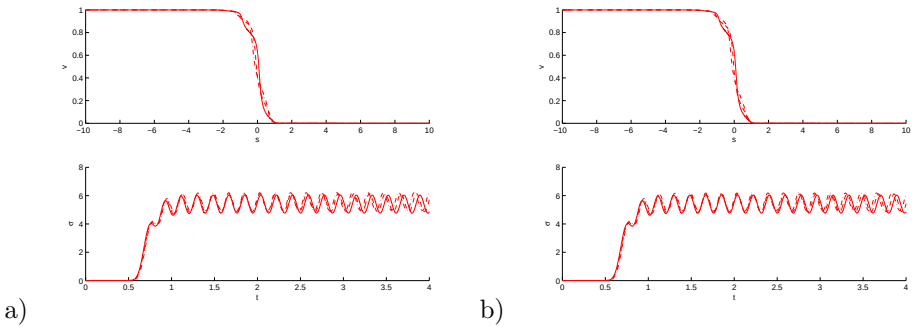

a) b)

FIG. 5.5. *Example 1. The numerical results of* $[s_l,s_r]=[-10,10]$, $t=4$ *and* $\Delta s=1/800$, $\epsilon=0.5$ *are presented. Top subplot gives the front shape* v^B *at time* $t=4$ *while the bottom subplot depicts the time evolution of* σ^B. *The dash dotted, dashed, and solid lines are respectively the numerical results of* $\Delta t=1/200$, $\Delta t=1/400$, *and the "exact" solution. a) The upwind method. b) The centered finite difference method.*

Δs	Δt	$\|E_{ct}\|_1$	c_{ct}	$\|E_{up}\|_1$	c_{up}
1/800	1/100	$3.5*10^{-2}$	6.0087	$3.7*10^{-2}$	5.6960
1/800	1/200	$1.8*10^{-2}$	5.6878	$2.1*10^{-2}$	5.5596
1/800	1/400	$8.9*10^{-3}$	5.5366	$1.2*10^{-2}$	5.4875
1/800	1/800	$4.1*10^{-3}$	5.4645	$7.2*10^{-3}$	5.4496

TABLE 5.2. *Example 1 of space periodic pulsating front. For different* Δt, *the numerical results of (3.16) and* (3.19) *with* $[s_l,s_r]=[-10,10]$, $\Delta s=1/800$, *and* $\epsilon=0.5$ *are presented. Here* $\|E\|_1$ *is the discrete* L^1 *norm and the subscripts "up" and "ct" are respectively the results of the upwind method and the centered finite difference method.*

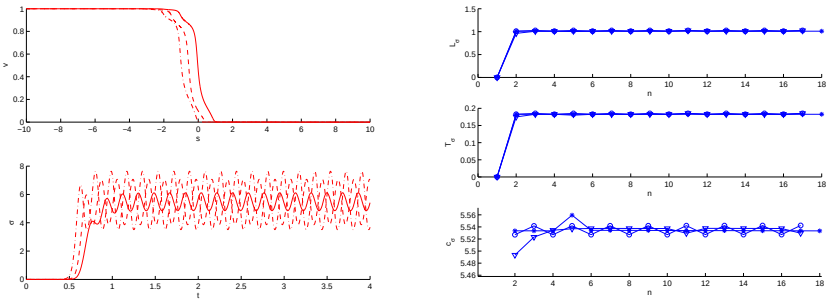

FIG. 5.6. *Example 1 of space periodic pulsating front for different* ϵ. *Left: Top subplot gives the front shape* v^B *at time* $t=4$ *while the bottom subplot depicts the time evolution of* σ^B. *The dash dotted, dashed and solid lines are the results of* $\epsilon=0.01$, 0.1, *and* 0.5, *respectively. Right: The numerical* L_σ *(top),* T_σ *(middle), and* c_σ *(bottom) for each period. Stars, circles, and triangles are for* $\epsilon=0.01$, 0.1, *and* 0.5, *respectively. The lines in the* c_σ *plot look apart from each other due to the short y-axis. Here we use* $\Delta s=1/400$, $\Delta t=1/400$.

v) The effect of computational domain: For $[s_l,s_r]=[-5,5]$, $[-10,10]$, and $[-20,20]$, we carry out the calculation using $\epsilon=0.5$, $\Delta s=1/400$, and $\Delta t=1/400$. For different computational domains, starting from the same initial data, the shapes of v^B for a fixed time and the evolution of σ^B are almost the same. Besides, the numerical

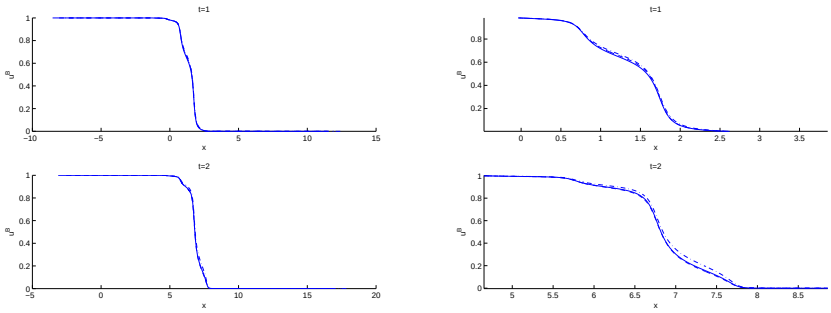

FIG. 5.7. *Example 1 of space periodic pulsating front for different* ϵ. *Left:* $u^B(x,t)=v^B(s+\int_0^t \sigma^B(\tau)d\tau,t)$ *are displayed for* $t=1$ *(top) and* $t=2$ *(bottom). Right: The magnification of the left figure. The dash dotted, dashed, and solid lines are the results of* $\epsilon=0.01,\ 0.1,$ *and* 0.5, *respectively. Here we use* $\Delta s=1/400,\ \Delta t=1/400$.

L_σ, T_σ, and c_σ for each period are the same for different computational domains as well, and therefore as long as the computational domain is larger than the transit region of the two limiting steady states.

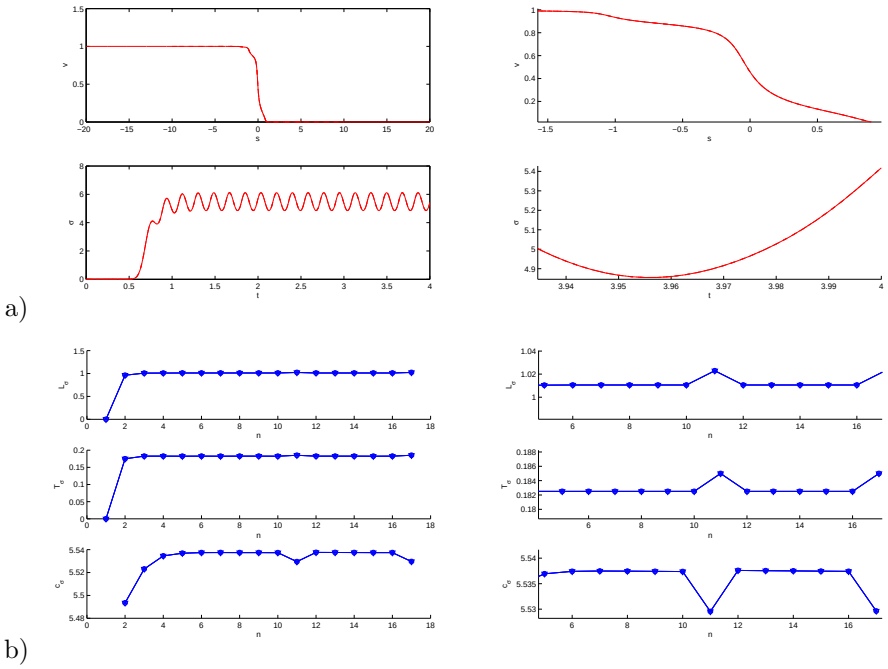

FIG. 5.8. *Example 1 of space periodic pulsating front for different computational domains. a): The profile of* $v^B(s,4)$ *and the evolution of* σ^B *with respect to time. The dash dotted, dashed, and solid lines are the results of* $[s_l,s_r]=[-5,5],\ [-10,10],$ *and* $[-20,20]$ *respectively, The right two subplots are the amplification of the left two subplots. Even if we zoom in, the results are so close to each other that we can not distinguish between them. b): The numerical* L_σ, T, *and* c_σ *for each period. The stars, circles, and triangles are for* $[x_l,x_r]=[-5,5],\ [-10,10],$ *and* $[-20,20]$ *respectively. The right three subplots are the amplification of the left three subplots. Here we use* $\epsilon=0.5,\ \Delta s=1/400,$ *and* $\Delta t=1/400$.

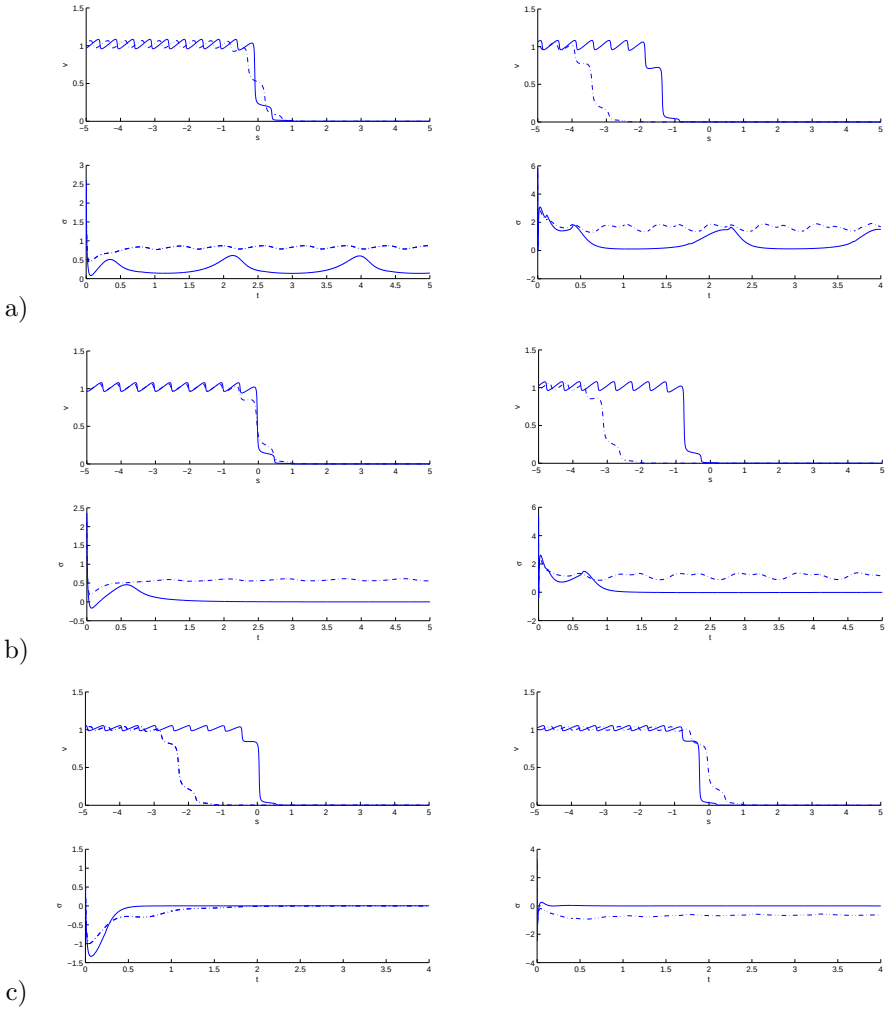

FIG. 5.9. *Example 2 of bistable space periodic pulsating fronts for different* η. *a)* $\eta=0.3$*; b)* $\eta=0.36$*; c)* $\eta=0.67$. *Left: The results of using the operator* $\mathfrak{P}_r$. *Right: The results of using the operator* $\mathfrak{P}_l$. *In each figure, the top subplots depict* $v^B(s)$ *at the specific time* $t=4$ *and the bottom subplots give the time evolution of* $\sigma^B(t)$. *Here the dash dotted and solid lines are respectively the results of* $\xi=0.9$ *and* $\xi=0.99$. *Quenching occurs when* $\eta=0.36$, $\xi=0.99$ *and* $\eta=0.67$, $\xi=0.99$, *i.e. the traveling velocities become zero. Here we use* $[s_l,s_r]=[-5,5]$, $\epsilon=0.5$ *and* $\Delta s=1/200$, $\Delta t=1/1000$.

Example 2: For the combustion reaction, the existence of pulsating front solutions has already been established by J.X. Xin [31, 32]. The numerical scheme we have developed here can be applied to more general reaction terms. It provides a tool for investigating the existence of pulsating front solutions. In this example, we investigate the bistable reaction. Let $\xi,\eta\in(0,1)$ and let the coefficients periodically depend on x, such that

$$\begin{aligned} &A(x)=1+\xi\cos(4\pi x), \qquad q(x)=0,\\ &f(x)=20u\big(1+0.4*\sin(4\pi x)-u\big)(u-\eta), \quad \text{for } x\in[0,1]. \end{aligned} \tag{5.2}$$

In [33], the author illustrates the quenching phenomenon for a bistable nonlin-

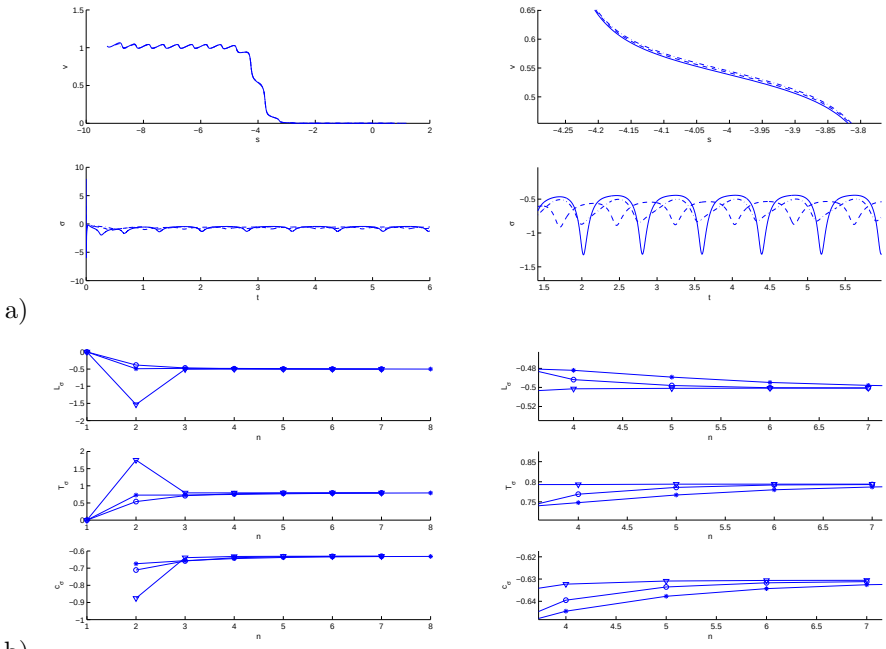

FIG. 5.10. *Example 2 of bistable space periodic pulsating fronts for different* ϵ *with* $\eta=0.67$, $\xi=0.9$. *a) The top subplots depict* $v^B(s)$ *at the specific time* $t=4$ *and the bottom subplots give the time evolution of* $\sigma^B(t)$. *Here the dash dotted, dashed, and solid lines are respectively the results of* $\epsilon=0.3$, 0.5, *and* 0.8. *b) The numerical* L_σ, T, *and* c_σ *for each period. The stars, circles, and triangles are for* $\epsilon=0.3$, 0.5, *and* 0.8, *respectively. The right three subplots are the amplification of the left three subplots. Here we have used* $\Delta s=1/200$, $\Delta t=1/1000$, *and chosen the operator* $\mathfrak{P}_l$.

Δt	Δs	$\|E_{ct}\|_\infty$	c_{ct}	$\|E_{up}\|_\infty$	c_{up}
1/1000	1/25	$1.25*10^{-2}$	8.750	$2.43*10^{-2}$	9.52
1/1000	1/50	$5.39*10^{-3}$	8.775	$1.24*10^{-2}$	9.16
1/1000	1/100	$1.99*10^{-3}$	8.781	$6.15*10^{-3}$	8.97
1/1000	1/200	$4.83*10^{-4}$	8.782	$2.95*10^{-3}$	8.87
1/100	1/400	$9.75*10^{-3}$	8.92	$1.03*10^{-2}$	8.96
1/200	1/400	$4.96*10^{-3}$	8.84	$5.58*10^{-3}$	8.89
1/400	1/400	$2.29*10^{-3}$	8.80	$2.96*10^{-3}$	8.85

TABLE 5.3. *Example 3 of time periodic pulsating front. For different* Δs, Δt *the numerical results of* (4.4) *and* (4.5) *with* $[s_l,s_r]=[-5,5]$, $\epsilon=0.5$ *are presented. Here* $\|E\|_\infty$ *is the discrete* L^∞ *norm and the subscripts "up" and "ct" respectively represent the results of the upwind method and centered finite difference method.*

earity such that $f(u)=u(1-u)(u-\eta)$ with $\eta\in(0,1/2)$. The quenching phenomenon indicates that the solutions are localized in space and there is no wave propagation. It depends on the degree of spatial inhomogeneity and can be observed by tuning the value of η [33]. The two steady states in [33] are uniform, while here we have a nonuniform limiting state. In [4], the existence of a nonuniform limiting state $p(x)$ and pulsating traveling front that connects $p(x)$ to zero is proved for $f(u)=u(\kappa(x)-u)$ with $\kappa(x)$ periodic in x. We will investigate the existence of pulsating fronts and the

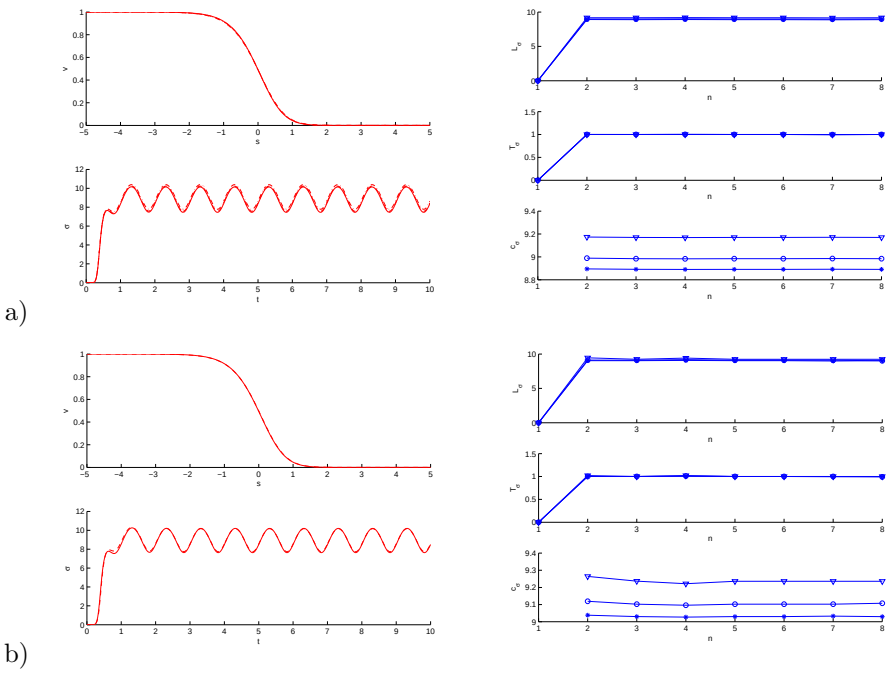

FIG. 5.11. *Example 3 of time periodic pulsating front. The numerical results of upwind method with* $\epsilon = 0.5$ *are presented. a) The results of* $\Delta t = 1/500$ *for different* Δs*. b) The results of* $\Delta s = 1/100$ *for different* Δt*. Left:* $v^B(s)$ *at the specific time* $t = 10$ *(top) and the evolution of* $\sigma^B(t)$ *(bottom). Dash dotted, dashed, and solid lines are for* $\Delta s = 1/50$, $1/100$, *and* $1/200$ *(*$\Delta t = 1/50$, $1/100$, *and* $1/200$*) respectively. These three lines are so close to each other that we can not distinguish them. Right: The numerical* L_σ *(top),* T *(middle), and* c_σ *(bottom) for each period. Triangles, circles, and stars are for* $\Delta s = 1/50$, $1/100$, *and* $1/200$ *(*$\Delta t = 1/50$, $1/100$, *and* $1/200$*) respectively. Unlike the space periodic case, the results of different mesh sizes and time steps are too close to each other to distinguish them.*

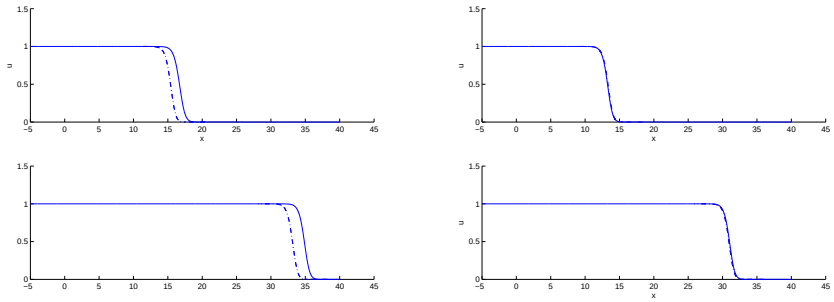

FIG. 5.12. *Example 3 of time periodic pulsating front. To compare our scheme with the direct time evolutionary simulation, we show the results of the direct time evolutionary simulation* $\tilde{u}^B$ *(solid lines) when* $t = 2$ *(top) and* $t = 4$ *(bottom) and the* u^B *recovered from* v^B *(dash dotted lines). Left: Upwind method. Right: Centered finite difference method.* $\tilde{u}^B$ *and* u^B *are so close to each other that we can not distinguish between them. Here we use* $\Delta s = 1/200$, $\Delta t = 1/400$, *and* $\epsilon = 0.5$.

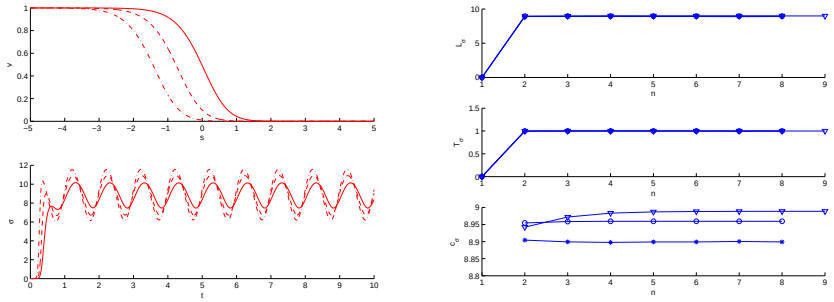

FIG. 5.13. *Example 3 of time periodic pulsating front for different* ϵ. *The numerical results using the upwind method,* $[s_l, s_r] = [-5, 5]$, *and* $\Delta s = 1/200$, $\Delta t = 1/400$ *are presented. Left:* $v^B(s)$ *at the specific time* $t = 10$ *(top) and the evolution of* $\sigma^B(t)$ *(bottom). Dash dotted, dashed, and solid lines are for* $\epsilon = 0.01,\ 0.1,$ *and* 0.5 *respectively. Right: The numerical* L_σ *(top),* T_σ *(middle), and* c_σ *(bottom) for each period. Triangles, circles, and stars are for* $\epsilon = 0.01,\ 0.1,$ *and* 0.5 *respectively.*

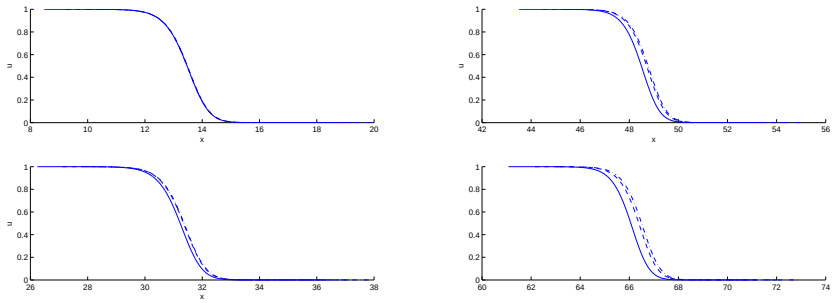

FIG. 5.14. *Example 3 of time periodic pulsating front for different* ϵ. *Dash dotted, dashed, and solid lines are for* $\epsilon = 0.01,\ 0.1,$ *and* 0.5 *respectively. Left:* $u^B(s)$ *recovered from* $v^B(s)$ *at the specific time* $t = 2$ *(top) and* $t = 4$ *(bottom). Right:* $u^B(s)$ *recovered from* $v^B(s)$ *at the specific time* $t = 6$ *(top) and* $t = 8$ *(bottom). Here we calculated with* $[s_l, s_r] = [-5, 5]$, $\Delta s = 1/200$, *and* $\Delta t = 1/400$.

quenching phenomenon for a bistable reaction-diffusion equation with nonuniform limiting states.

When "quenching" occurs, since the front stops at a certain position which is not necessarily near 0, we start from front-like initial data with front position near zero:

$$v^{B0} = \begin{cases} 1, & s, \in [s_l, -1], \\ \frac{e^{-(x+1)^2} - e^{-4}}{1 - e^{-4}}, & s \in [-1, 1], \\ 0, & x \in [1, s_r]. \end{cases}$$

The numerical results of different η and ξ are displayed in figure 5.9. We can see that the bigger the variations of the coefficients from their mean states, i.e. the bigger ξ is in our case, then the smaller the absolute values of the traveling velocities are. Quenching occurs when η is close to $1/2$ and the variations of $A(x)$ from its mean states are big, even if the limiting states are not uniform. We observe numerically the existence of pulsating traveling fronts that connect a nonuniform limiting state to zero when η is away from $1/2$. Moreover, the traveling velocity is negative when η is away from and bigger than $1/2$, and positive when η is away from and less than $1/2$. This is similar to the Allen-Cahn model [24].

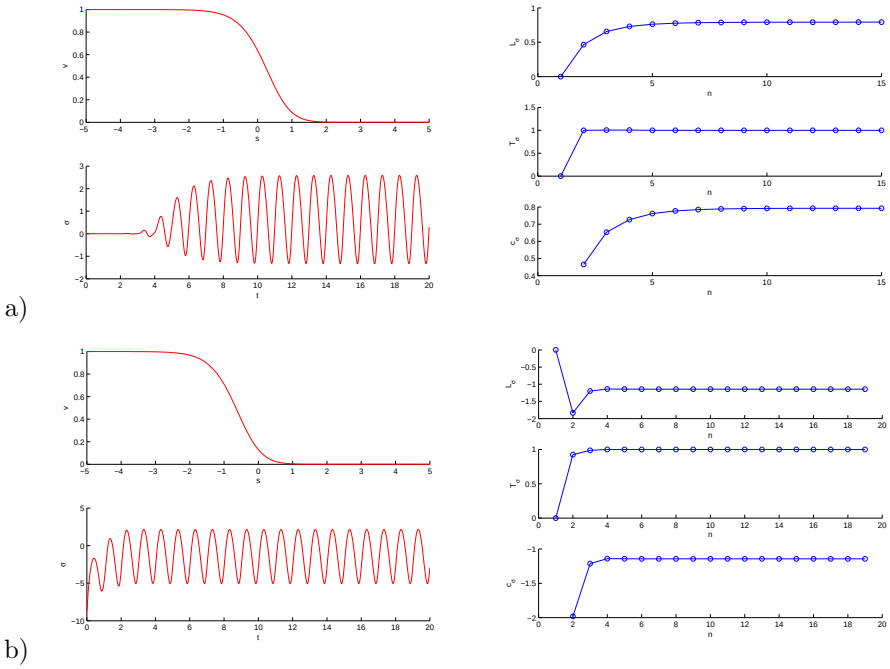

FIG. 5.15. *Example 3 of time periodic pulsating front for different* α. *a)* $\alpha=-8$. *b)* $\alpha=-10$. *Left:* $v^B(s)$ *at the specific time* $t=10$ *(top) and the evolution of* $\sigma^B(t)$ *(bottom). Right: The numerical* L_σ *(top),* T *(middle), and* c_σ *(bottom) for each period.*

The different results in the left and right figures in figure 5.9 illustrate the necessity of different choice of $\mathfrak{P}$. The column on the left hand side displays the numerical results of using $\mathfrak{P}_r$. We see that when c is positive (case (a) $\eta=0.3$) or when quenching occurs (case (b) $\eta=0.36$), $\mathfrak{P}_r$ can confine the front position around zero, while when c is negative (case (c) $\eta=0.67$), the front of $v(s,t)$ moves to the left and $\sigma(t)$ converges to zero. In the right hand side column of figure 5.9, the numerical results of using $\mathfrak{P}_l$ are shown. When c is negative or when quenching occurs, the front positions of $v(s,t)$ are confined, while they move to the left when c is positive. In summary, when quenching occurs both $\mathfrak{P}_r$ and $\mathfrak{P}_l$ can be employed, while when $c>0$, only $\mathfrak{P}_r$ can achieve the front confinement, and when $c<0$, only $\mathfrak{P}_l$ can. Numerically, if the sign of c is not known a priori, we need to try both $\mathfrak{P}_r$, $\mathfrak{P}_l$, but in most problems under consideration, it is not difficult to determine the sign of c by looking at the propagation direction of the original time evolutionary equation.

The numerical results in figure 5.10 show that when $\eta=0.67$, $\xi=0.9$, and the operator $\mathfrak{P}_l$ is employed, different ϵ provide almost the same u^B. Similar to example 1, different ϵ give different $\sigma(t)$, but the same L_σ, T_σ, and c_σ. Moreover, when "quenching" occurs, $\sigma(t)$ converges to 0 no matter which ϵ is used.

Example 3: In this example we test the performance of our scheme for the time periodic advection diffusion reaction equation (1.3). Choose

$$A(t)=1+0.8\sin(2\pi t), \qquad q(t)=\alpha+0.5\cos(2\pi t), \qquad f(t,u)=20u(1-u). \tag{5.3}$$

Here $f(t,u)$ is KPP type for which the pulsating traveling front is not unique [20]. However, if we use the boundary condition $v(s_r)=0$, we expect to find the front

with minimum velocity. This is true for the traveling wave simulations, since when $f[u]=u(1-u)$ in (1.6), the traveling wave solution with minimum velocity is found when passing to the limit $x_{r,l}\to\pm\infty$ [7]. For the more general time periodic equation (1.3), a pulsating traveling front can be found by setting $v(s_r)=0$. To rigorously prove that this provides the minimum velocity pulsating traveling front, and the design of boundary conditions for other faster fronts, will be the subject of future work. The purpose of this paper is to show the performance of the numerical scheme.

Letting $\alpha=0$ in (5.3), we will illustrate the scheme convergence and its independence with respect to ϵ, as well as verify that the solution of the original time evolutionary equation can be recovered. Then for different choices of α, we test the effect of advection and verify that the sign of c is a sufficient condition to determine which operator, $\mathfrak{P}_l$ or $\mathfrak{P}_r$, to choose.

Scheme convergence: Unlike the space periodic case, figure 5.11 shows space and time convergence for both v^B and σ^B. The period of σ does not depend on Δs and Δt. Here only the numerical results of the upwind method are displayed since the centered finite difference method produces similar pictures. Furthermore, we can see in table 5.3 the first order space convergence for the upwind method, the second order space convergence for the centered finite difference method, and the first order convergence in time for both methods. In all the calculations, we use $[s_l,s_r]=[-5,5]$ and $\epsilon=0.5$.

Comparison with direct time evolutionary simulations: We can implement the direct time evolutionary simulations by letting $\sigma^{Bn}=0$ in (4.4) or (4.5) and using a larger computational domain. From figure 5.12, we can see that, due to the numerical diffusion, the front position recovered from the solution of the upwind method (4.4) is different from the $\tilde{u}^B$ that is obtained from direct time evolutionary simulation. However, when we refine the mesh, first order convergence can be found in its L^1 norm. The centered finite difference method introduces no numerical diffusion. The $\tilde{u}^B$ and u^B recovered from v^B are so close to each other that we can not distinguish between them. Here we use $\Delta s=1/200$, $\Delta t=1/400$, and $\epsilon=0.5$.

The independence of ϵ: The numerical results of $\epsilon=0.01$, 0.1, and 0.5 using the upwind method are presented in figure 5.13. The centered finite difference method gives similar results. We can see that different ϵ give different $v^B(s,10)$ and $\sigma^B(t)$. Since the original (1.3) is independent of ϵ, at the discrete level, the u^B recovered from v^B should also be independent of ϵ. From figure 5.14, for given t, different ϵ give the same front position, and although the numerical errors depend on ϵ and increase linearly, they can be diminished by refining the mesh.

The effect of α: In the space periodic examples, the $q(x)$ in all tests satisfy $\int_0^L q(x)\,dx=0$, while when $\alpha=0$ in the present time periodic example, we also have $\int_0^T q(t)\,dt=0$. We test the case when $\int_0^T q(t)\,dt\neq 0$ by choosing $\alpha=-8$ and -10. The numerical results are presented in figure 5.15. For both values of α, $\sigma(t)$ changes its sign during the time evolution. To have confinement of the front position, numerically, we have to use $\mathfrak{P}_r$ for $\alpha=-8$ and $\mathfrak{P}_l$ for $\alpha=-10$. This observation confirms that the determinant condition of choosing $\mathfrak{P}_l$ or $\mathfrak{P}_r$ is the sign of c, and not $\sigma(t)$ itself.

6. Conclusion

In this paper, we propose a relaxation method for the simulations of pulsating traveling fronts which is applicable to space or time periodic advection diffusion reaction equations.

The pulsating traveling fronts are an extension of traveling waves, for which the front shapes and traveling velocities change periodically in time. The idea of this new method is to find both $\sigma(t)$ and $v(x-\int_0^t \sigma(\tau)d\tau,t)$ that are periodic in time, which can be achieved by solving (2.3) for the space periodic equation and (2.4) for the time periodic equation, with $\mathfrak{P}$ chosen as in (3.11).

This new method is an extension of the relaxation scheme proposed in [27] for one dimensional traveling wave simulations. It has several advantages. Firstly, only a small computational domain is required, which reduces the computational cost when the convergence to the pulsating front solution is slow; this advantage would be more important for high dimensional pulsating front simulations. Secondly, the front velocity can be found automatically, and is a crucial physical variable, but not easy to obtain in direct time evolutional simulations. Finally, we can recover the solution of the original time evolutional equation by $u(x,t)=v(x-\int_0^t \sigma(\tau)d\tau)=v(s,t)$.

We show the implementation of our scheme to the combustion reaction with ignition temperature, the bistable reaction for the space periodic advection diffusion reaction equation, and the Fisher/KPP reaction for the time periodic advection diffusion equation. The numerical diffusion introduced by discretizing the advection term leads us to overestimate the propagation velocity, but the L^1 convergence of the front can be found when we refine the mesh. The front velocity $c=L/T$ converges to a constant for pulsating front solutions. For the bistable reaction term, we can verify the quenching phenomena and existence of pulsating fronts that connect the nonuniform limiting state to zero. Since it is much easier to justify the periodic changes without propagation than with propagation, this scheme can be used as a tool for exploring and verifying the existence of pulsating traveling fronts and finding the front velocity.

Several interesting questions require more detailed analysis, for instance, whether the steady states of the time periodic advection diffusion reaction equation are always uniform in space and whether the pulsating traveling front we have found in Example 3 has the minimum velocity. Moreover, for the spatial-temporal periodic advection reaction diffusion equation, it is not clear whether we obtain a pulsating front or not, even if $(v(s,t),\sigma(t))$ becomes periodic in t. However, the purpose of this paper is to present an efficient numerical scheme for finding pulsating traveling fronts. All the above questions, as well as the higher dimensional extensions, will be the subject of future papers.

REFERENCES

[1] H. Berestycki, *The influence of advection on the propagation of fronts in reaction-diffusion equations*, Nonlinear PDEs in Condensed Matter and Reactive Flows, NATO Science Series, H. Berestycki and Y. Pomeau (eds.), 569(1), 11–48, 2003.

[2] H. Berestycki and F. Hamel, *Front propagation in periodic excitable media*, Commun. Pure Appl. Math., 55, 949–1032, 2002.

[3] H. Berestycki, F. Hamel, and L. Roques, *Analysis of the periodically fragmented environment model: I. Influence of periodic heterogeneous environment on species persistence*, J. Math. Biol., 51, 75–113, 2005.

[4] H. Berestycki, F. Hamel, and L. Roques, *Analysis of the periodically fragmented environment model: II. C biological invasions and pulsating travelling fronts*, J. Math. Pures Appl., 84(8), 1101–1146, 2005.

[5] H. Berestycki and F. Hamel, *Generalized travelling waves for reaction-diffusion equations*, Perspectives in Nonlinear Partial Differential Equations, H. Brezis, H. Berestycki et al. (eds.), Contemp. Mathematics, Amer. Math. Soc., Providence, RI., 446, 101–123, 2007.

[6] H. Berestycki, B. Larrouturou, and J.-M. Roquejoffre, *Mathematical investigation of the cold boundary difficulty in flame propagation theory*, Institute for Mathematics and Its Applications, Springer, New York, 35, 37–61, 1991.

[7] H. Berestyski, B. Nicolaenko, and B. Scheurer, *Traveling wave solutions to combustion models and their singular limits*, SIAM J. Math. Anal., 16(6), 1207–1242, 1985.
[8] R.A. Fisher, *The Genetical Theory of Natural Selection*, Clarendon Press, 1930. Second Edition: Dover, 1985. Third Edition, Oxford Univ. Press, 1999.
[9] G. Frejacques, *Traveling Waves in Infinite Cylinders with Time-Periodic Coefficients*, Universit é Aix-Marseille, PhD thesis, 2006.
[10] M.I. Freidlin, *Propagation of a concentration wave in the presence of random motion associated with the growth of a substance*, Soviet Math. Dokl., 20, 503–507, 1979.
[11] M.I. Freidlin, *Functional Integration and Partial Differential Equations*, Ann. Math. Stud., Princeton University Press, Princeton, NJ, 109, 1985.
[12] W. Hudson and B. Zinner, *Existence of travelling waves for reaction-diffusion equations of Fisher type in periodic media*, Boundary Value Problems for Functional-Differenctial Equations, J. Henderson (ed.), World Scientific, 187–199, 1995.
[13] W. Hundsdorfer, *Numerical Solution of Advection-Diffusion-Reaction Equations*, Lecture notes at the Thomas Stieltjes Institute, 2000.
[14] V. Hutson, K. Michaikow, and P. Polacik, *The evolution of dispersal rates in a heterogeneous time-periodic environment*, J. Math. Biol., 43, 501–533, 2001.
[15] S. Jin and X. Wen, *An efficient method for computing hyperbolic systems with geometrical source terms having concentrations*, J. Comput. Math., 22, 230–249, 2004.
[16] R.J. LeVeque, *Balancing source terms and flux gradients in high-resolution Godunov methods: The quasi-steady wave-propagation algorithm*, J. Comput. Phys., 146, 346–365, 1998.
[17] J. Nolen and J. Xin, *Reaction diffusion front speeds in spacially-temporally periodic shear flows*, SIAM J. Multiscale Model. Sim., 1(4), 554–570, 2003.
[18] J. Nolen and J. Xin, *Existence of KPP type fronts in space-time periodic shear flows and study of minimal speeds based on variational principle*, Dis. Cont. Dyn, Syst., 13, 1217–1234, 2005.
[19] G. Nadin, *Existence and uniqueness of the solutions of a space-time periodic reaction-diffusion equation*, J. Diff. Eqs., 249(6), 1288–1304, 2010.
[20] G. Nadin, *Traveling fronts in space-time periodic media*, J. Math. Pures Appl., 92, 232–262, 2009.
[21] G. Nadin, *Pulsating traveling fronts in space-time periodic media*, C.R. Acad. Sci. Paris I, 346, 951–956, 2008.
[22] G. Nadin, B. Perthame, and M. Tang, *Can a traveling wave connect two unstable states? The case of the nonlocal Fisher equation*, Comptes Rendus Mathematique, Paris, 349(9-10), 553–557, 2011.
[23] B. Perthame and C. Simeoni, *A kinetic scheme for the Saint-Venant system with a source term*, CALCOLO, 38(4), 201–231, 2001.
[24] B. Perthame, *Transport Equations in Biology*, Frontiers in Mathematics, Basel: Birkhäuser Verlag, 2007.
[25] N. Shigesada and K. Kawasaki, *Biological Invasions, Theory and Practice*, Oxford Univ. Perss, Oxford, 1997.
[26] N. Shigesada, K. Kawasaki, and E. Teramoto, *Traveling periodic waves in heterogeneous environments*, Theoretical Population Biology, 30, 143–160, 1986.
[27] W.R. Sun and M. Tang, *A new relaxation method for one dimensional traveling wave simulations*, submitted.
[28] W. Shen, *Tranveling waves in time almost periodic structures governed by bistable nonlinearities, 1. Stablity and uniqueness*, J. Diff. Eqs., 159, 1–55, 1999.
[29] W. Shen, *Traveling waves in time almost periodic structures governed by bistable nonlinearities, 2. Existence*, J. Diff. Eqs., 159, 55–101, 1999.
[30] H. Weinberger, *On spreading speed and traveling waves for growth and migration models in a periodic habitat*, J. Math. Biol., 45, 511–548, 2002.
[31] J.X. Xin, *Existence and uniqueness of traveling waves in a reaction-diffusion equation with combustion nonlinearity*, Indiana Univ. Math. J., 40, 985–1008, 1991.
[32] J.X. Xin, *Existence of planar flame fronts in convective-diffusive periodic media*, Arch. Rat. Mech. Anal., 121, 205–233, 1992.
[33] J.X. Xin, *Existence and nonexistence of traveling waves and reaction-diffusion front propagation in periodic media*, J. Statist. Phys., Springer, 73, 893–926, 1993.